Doctoral Dissertations and Master's Theses

Summer 7-25-2023

The Influence of Mixing Duct Length and Phase of Flight on Wall Temperatures of a Rocket Based Combined Cycle Engine in Ejector and Air-Augmented Modes

Jonathan Grow
Embry-Riddle Aeronautical University, growj@my.erau.edu

Follow this and additional works at: https://commons.erau.edu/edt

Part of the Aerodynamics and Fluid Mechanics Commons, Heat Transfer, Combustion Commons, Propulsion and Power Commons, and the Space Vehicles Commons

Scholarly Commons Citation

Grow, Jonathan, "The Influence of Mixing Duct Length and Phase of Flight on Wall Temperatures of a Rocket Based Combined Cycle Engine in Ejector and Air-Augmented Modes" (2023). *Doctoral Dissertations and Master's Theses*. 755.
https://commons.erau.edu/edt/755

This Thesis - Open Access is brought to you for free and open access by Scholarly Commons. It has been accepted for inclusion in Doctoral Dissertations and Master's Theses by an authorized administrator of Scholarly Commons. For more information, please contact commons@erau.edu.

ACKNOWLEDGMENTS

I would like to express my gratitude to my advisor, Dr. Ricklick, for your patience and guidance throughout the creation of this thesis. Thank you for welcoming my obsession with rocketry into your lab and for putting me on the path to success.

I would also like to thank my committee members Dr. Narayanaswami and Dr. Boetcher for their words of encouragement and insightful comments that helped shape this thesis.

To the many friends and colleagues that I have made during my time at Embry-Riddle, thank you for your kindness and friendship over the years. To the students of the Gas Turbine Lab and fellow graduate students, I cannot thank you enough for answering all of my questions and helping me when I needed it most. This thesis would not have been possible without the knowledge, wisdom, and comradery of my peers. I cannot begin to list everyone who positively impacted me during my time at Embry-Riddle, but I believe you know who you are.

Last, but most importantly, I would also like to thank my parents and brother for their love and support over the years through good times and bad. It seems that I've come a long way since our trips to the Air and Space Museum and Sunday model rocket launches at the Goddard Space Flight Center. Without all of you, I would never have made it this far.

ABSTRACT

Rocket Based Combined Cycle (RBCC) engines have been theorized as a possible means of powering launch vehicles and high-speed atmospheric vehicles. By incorporating aspects of both air-breathing and rocket propulsion, RBCC engines promise up to a 230 % increase in specific impulse over traditional chemical rocket propulsion by entraining a secondary flow of atmospheric air and mixing it with the exhaust of a rocket motor. Students within the Embry-Riddle Future Space Explorers and Developers Society (ERFSEDS) identified a problem of excessive heating and structural failure of the mixing duct during launch and transonic flight of a student-built flight test vehicle. In order to be a feasible means of propulsion, adequate cooling of the mixing duct is necessary to achieve long burn times. Research revealed a lack of studies on the thermal trends and cooling of RBCC engine mixing ducts in the non-classified literature. This study utilized computational fluid dynamics (CFD) to analyze the flow mixing behavior and resulting thermal trends on the walls of the mixing duct. The two parameters investigated were the effects of varying the mixing duct length to diameter (L/D) ratio as well as the effects of different phases of flight on the thermal trends within the mixing duct. Launch, transonic, supersonic, and high-altitude cases were all selected from a reference trajectory. Additionally, the interaction between the entrained secondary flow of air and the mixing duct walls was of interest to see if the secondary flow had a natural capacity to film cool the mixing duct walls. Thermal trends within the mixing duct were characterized through the analysis of wall temperatures, wall heat transfer coefficient, and film cooling effectiveness. Additionally, contour plots were used to qualitatively evaluate internal flow behaviors. After modelling was completed, it was discovered that increasing mixing duct L/D to values over 7 resulted in greater flow mixing, but heightened thermal stresses on the mixing duct. Following analysis the four different phases of flight, it was determined that the high-altitude phase of flight posed the highest thermal stresses on the mixing duct with 79.6 % higher peak wall temperatures and 67.5 % higher heat transfer coefficients compared to the supersonic case, which posed the lowest thermal stresses. This study indicates that RBCC engine designs should avoid long mixing ducts and flight conditions with highly under-expanded primary flows that promote harsh thermal conditions.

TABLE OF CONTENTS

LIST OF FIGURES

LIST OF TABLES

NOMENCLATURE

$\dot{m}$	Mass Flow Rate
η	Adiabatic Film Cooling Efficiency
γ	Ratio of Specific Heats
μ_∞	Freestream Dynamic Viscosity
ϕ	Thrust Augmentation
ρ_∞	Freestream Density
v_∞	Freestream Velocity
2D	Two Dimensional
w_P	Mass Flow Rate of Primary Flow
w_S	Mass Flow Rate of Secondary Flow
τ_w	Wall Shear Stress
$\mathrm{A^*}_P$	Primary Flow Area at Nozzle Exit Plane in Choked Condition
A_{1S}	Secondary Flow Area at Nozzle Exit Plane
c	Characteristic Length
CFD	Computational Fluid Dynamics
DNS	Direct Numerical Simulation
F	Thrust
g_0	Standard Acceleration Due to Gravity
I_{sp}	Specific Impulse

I_t	Total Impulse
L/D	Length to Diameter Ratio
LES	Large Eddy Simulation
M	Mach Number
M_c	Convective Mach Number
P	Static Pressure
P_0	Total Pressure
P_{0P}	Total Pressure of Primary Flow
P_{0S}	Total Pressure of Secondary Flow
R	Gas Constant of Air
RANS	Reynolds-Averaged Navier Stokes
RBCC	Rocket-Based Combined Cycle
Re	Reynolds Number
SSTO	Single-Stage-to-Orbit
T	Static Temperature
T_0	Total Temperature
$\mathrm{T}_{w,ad}$	Adiabatic Wall Temperature
v	Velocity

1 Introduction

Chemical rocket propulsion is a marvel of modern engineering. It is currently the only means of lifting and accelerating orbital launch vehicles from the surface of the Earth and into space. Though chemical rockets are powerful machines, they are inefficient when compared to air-breathing propulsion devices such as gas turbines, ramjets, and scramjets. This inefficiency is caused by a fundamental characteristic of chemical rocket propulsion; while air-breathing engines use the oxygen within the air to burn fuel and create thrust, rocket engines must carry their oxidizer onboard in order to operate in the vacuum of space. In response to this problem, many concepts have been proposed to raise the efficiency of chemical rocket engines. One such concept is called Rocket Based Combined Cycle (RBCC) propulsion. Since the mid-20th century, RBCC engines have been studied as a possible means of increasing the capabilities of orbital launch vehicles and high-speed atmospheric flight. RBCC engines promise increases in efficiency over traditional chemical rocket propulsion by combining features of both air-breathing and chemical rocket propulsion into one system.

In 2019, the Embry-Riddle Future Space Explorers and Developers Society (ERFSEDS) constructed a series of small RBCC-powered flight vehicles to test the effect of mixing duct length on flight performance. Named Gryphus, the team constructed the third iteration of their vehicle designed called Gryphus III. Shown in Figure 1.1, this was designed to be a transonic flight vehicle. It featured four NACA duct inlets that fed air into a mixing duct where air would be mixed with rocket exhaust before exiting into the atmosphere. The mixing duct was designed to be removable, so that ducts of varying lengths could be used to see which length over diameter ($\frac{L}{D}$) ratio yielded the highest propulsive performance.

During the initial flight of Gryphus III, a mixing duct with an $\frac{L}{D}$ of 10 was used. Significant degradation of the vehicle's mixing duct was observed during launch and powered flight. This resulted in the loss of part of the duct and the attached fins that stabilized the

Figure 1.1 Gryphus III with extended and shortened mixing duct.

vehicle. Damage of this magnitude was not observed earlier in the project on the smaller ducted RBCC vehicles, Gryphus I and II. Thus, mixing duct failure was not considered in the design of Gryphus III. Following the post-flight recovery and analysis of Gryphus III, the team determined that significant heating of the mixing duct from the hot rocket exhaust caused it to be weakened and result in eventual structural failure.

The questions were then posed: 1. How does the mixing duct L/D affect the thermal conditions on the mixing duct walls? 2. What effects does the phase of flight have on thermal conditions imposed on the mixing duct walls. 3. Does the secondary flow entrained into the mixing duct have a natural capacity to cool the mixing duct walls? Subsequent research performed by the team found a lack of publicly available literature on thermal stresses or cooling methods specific to RBCC engines. Answering these questions would provide a more complete understanding of the thermal environment that an RBCC engine operates under and allow for future designs to be made that mitigate the effects of these thermal conditions.

In this investigation, a numerical model of the temperature and heat transfer trends on an RBCC engine's mixing duct is performed using computational fluid dynamics (CFD) to better understand how changes to mixing duct $\frac{L}{D}$ and phase of flight affect the thermal conditions inside an RBCC engine mixing duct.

1.1 Introduction to Chemical Rockets and Limitations

Chemical rockets are a type of propulsive device in which chemical energy stored in propellants is released through combustion in the form of high-pressure, high-temperature gases. These gases are then accelerated to very high velocity by the use of a nozzle [8]. The accelerated gases produce a reactionary force on the engine called thrust, which is then used to propel the vehicle that the chemical rocket is attached to. Chemical rocket engines are currently the only form of propulsion used for powering orbital launch vehicles.

There are two main types of chemical rocket engines used on atmospheric flight vehicles-solid propellant and liquid propellant rocket engines. These names describe the state of matter in which the propellants are stored in, prior to combustion. Solid propellant rocket motors are the simplest type and consist of a mixture of fuel and oxidizer, which are held together by a binder. This mixture is cast as a solid and called a propellant grain. During operation, this grain generates high-temperature, high-pressure exhaust gases. Solid propellant motors generally find use as first-stage boosters due to their high thrust capability. Liquid-propellant rocket engines store liquid propellants in large tanks within the vehicle that are either pressure fed or pump fed to a thrust chamber for combustion. Liquid-propellant rocket engines find uses on first stages and upper stages of launch vehicles with many in-orbit applications with different propellant combinations used to maximize efficiency in different operating environments.

An important metric used to measure the efficiency of a rocket motor is called specific impulse (I_{sp}) and is calculated as follows.

$$I_{sp} = \frac{F}{\dot{m} g_0} = \frac{I_t}{m_p g_0} \tag{1.1}$$

Specific impulse (I_{sp}) the thrust force per unit "weight" flow rate of propellant [8]. It can also be described as the total impulse per unit weight of propellant [8]. In Equation 1.1, F is the thrust generated by the engine, $\dot{m}$ is the mass flow rate of propellant through the engine, and g_0 is the standard acceleration to due gravity at the surface of the Earth [8]. The unit for I_{sp} is seconds (s). The weight flow rate of propellant for a rocket engine includes both the onboard fuel and oxidizer for a rocket engine, while only the flow rate of the fuel is considered for an air-breathing engine. It is desirable for a chemical rocket engine to have the highest specific impulse possible. This results in a propulsion system produces a highest amount of thrust for a lowest mass of propellant.

Chemical rocket engines suffer from relatively low I_{sp} values when compared to air breathing propulsion such as gas turbines, ramjets, and scramjets. Conventional chemical rocket propulsion yields specific impulse values ranging from 200-468s [8]. This is largely because air-breathing propulsion utilizes the oxygen in the atmosphere to sustain combustion, where chemical rocket engines must carry both a fuel and oxidizer onboard. This results in large launch vehicles which, prior to launch, can be more than 91 % propellant by mass [8]. Because of this, it is a significant challenge to launch large payloads into space due to the large size of launch vehicles required. Low I_{sp} chemical rockets result in large multi-stage launch vehicles that drive higher costs for accessing space [9].

1.2 Introduction to Rocket Based Combined Cycle Propulsion

Rocket Based Combined Cycle (RBCC) propulsion is a category of propulsive devices which combine aspects of air breathing and rocket propulsion into one engine. RBCC engines generally feature a rocket engine which is surrounded by an inlet and duct so that air from the atmosphere can be ingested and mixed with the rocket's exhaust to raise the I_{sp} and thrust level above the rocket engine. Industry studies have shown potential specific impulse increases of up to 230% [10].

RBCC engines have several advantages over conventional chemical rocket engines. Whereas a typical chemical rocket engine will operate in one cycle with an essentially fixed I_{sp} from launch until the point where all propellant onboard has been depleted, RBCC engines are capable of transitioning to different operating modes during flight. This is enabled by combining attributes of air breathing engines and rockets into one engine. With this ability, RBCC engines allow for an optimal operating mode to be utilized to maximize efficiency at any flight Mach number and altitude. In the application of an orbital launch vehicle, an RBCC engine functions in the rocket-ejector mode during launch. Once the vehicle is supersonic, the air-augmented or ram-rocket mode [11]. At approximately Mach 3, the RBCC engine will switch to ramjet mode and use the oxidizer in the atmosphere to combust with the onboard fuel [9]. At approximately Mach 5, a scramjet mode will be used to further accelerate the vehicle at hypersonic Mach numbers and high altitudes. Once the vehicle has climbed to an altitude where there is an insufficient amount of oxygen in the atmosphere to sustain combustion, the RBCC engine will switch to a conventional chemical rocket engine operating mode until the vehicle reaches the desired velocity for orbital insertion [9].

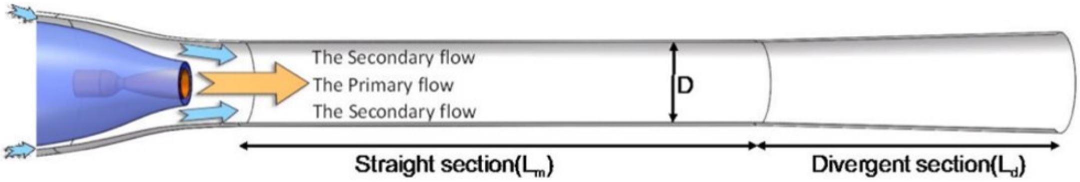

Figure 1.2 Cutaway of a simplified RBCC engine [1]

A RBCC engine consists of a few basic features- an inlet, rocket motor, and a mixing duct. During rocket-ejector mode, the rocket engine fires within the mixing duct. This creates a high-speed jet of rocket exhaust that called the primary flow. The primary flow has a pumping effect and this entrains and compresses a secondary flow of air from the inlet into the mixing duct [12]. The mixing of the primary and secondary flows inside the duct transfers momentum from the primary flow to the secondary flow [9]. This accelerates the secondary flow and increases its stagnation pressure [12]. The addition of the secondary flow raises the total mass flow rate through the mixing duct to include the sum of the rocket exhaust and secondary air. This results in a higher thrust level being generated than the reference rocket firing alone [13]. Experimental examples have found I_{sp} augmentation of 10-20 % over the reference rocket when operating at zero velocity and up to 230 % when operating at Mach 2-3 [10].

1.3 RBCC Engine Mixing Duct Design Considerations

In order for a RBCC engine to function properly, it must be designed to have adequate mixing duct length in order for the primary and secondary flows to mix. Prior experimentation has found that the ideal length to diameter ratio ($\frac{L}{D}$) for the mixing duct of a supersonic ejector to be 8.5 [10]. During normal operation, mixing of the primary and secondary flows in the duct allow for the hot rocket exhaust gases in the center of the duct to propagate outwards towards the duct wall. This will result in the duct wall being subjected to thermal stresses generated by the rocket exhaust in the mixing duct. At the beginning of the mixing duct, the primary and secondary flows are segregated. As the two flows travel down the mixing duct, the two flows should be fully mixed by the time the flows have reach the duct exit. The flow field is constantly developing under various stages of mixing as it travels down the length of the duct. Consequently, the heating of the duct walls is presumed to vary depending on the downstream location from the beginning of the mixing duct.

Different flight regimes encountered during a launch vehicle's ascent will result in significant changes in the inlet and mixing duct exit conditions due to changes in altitude and airspeed as the launch vehicle climbs through the atmosphere. The corresponding changes to the secondary flow inlet conditions caused by variations in velocity, pressure, temperature, and air density are all factors that must be considered. The significant changes in secondary flow conditions will have an impact on the effectiveness of the mixing duct and the resulting thermal stresses on the mixing duct walls.

1.4 Potential Utilization of Secondary Flow to Cool Mixing Duct Walls

During the post-flight research of thermal conditions and cooling methods of an RBCC mixing duct after the first flight of Gryphus III, two questions were asked. Does the secondary flow of air entering the mixing duct have a natural ability to cool the mixing duct walls? If the ingested secondary flow has the ability to passively cool the mixing duct walls could it possibly provide a number of benefits for the overall engine and vehicle? Also, could a mixing duct be designed to use the secondary flow to cool the mixing duct walls during powered flight?

This study will investigate whether the secondary flow can perform film cooling in which the secondary flow passing over the mixing duct wall can insulate the wall from the rocket exhaust of the primary flow and convect heat downstream and out of the mixing duct. If found to be possible, then this passive cooling method may yield potential benefits including weight savings and reduced complexity. If harnessed, this natural cooling effect could allow for the omission of heavy thermal management systems such as ablative heat shields, film cooling, or regenerative cooled walls. This could also reduce cost and help make RBCC engines a more cost-competitive propulsion option to power launch vehicles.

1.5 Modelling Thermal Trends to Improve Mixing Duct Design

The design of future RBCC engines should be done in a manner that minimizes the thermal stresses on a mixing duct that could lead to a structural failure, such as that of Gryphus III. The modeling of these thermal trends within the mixing duct is essential for painting a full picture of the problem before engineers can properly address the issue with thermal management devices and techniques such as ablatives, regenerative cooling, film cooling, or perhaps some novel cooling concept can be applied to an RBCC engine.

2 Literature Review

This literature review will review related sources to RBCC engine research as well as subjects pertaining to cooling of high speed propulsive devices. However, no publicly available sources detailing the thermal conditions within a RBCC engine mixing duct or its cooling are available at this time. Related literature will be presented to give more background and context to this study.

2.1 RBCC Engine Origins and Performance Analysis

Research and analysis on RBCC engines began in the 1960's as Rocket Based Combined Cycle (RBCC) engines were identified as the potential future of chemical rocket engine development. Up until this point, success was had with the large liquid propellant engines constructed for large launch vehicles, but the operational and fiscal limitations of these enormous, multi-stage, expendable launch vehicles were becoming apparent. In order to obtain regular and lower cost access to space, a more reusable orbital launch system would be needed. Fully reusable two-stage and Single-Stage-To-Orbit (SSTO) were hoped to be the solution that the industry needed to improve access to space [14]. A new generation of highly efficient propulsive devices would be needed in order to power these vehicles. As a result, studies were commissioned by various government agencies and the Department of Defense in order to gauge the possible performance and feasibility of RBCC propulsion.

Currently, no type of propulsion system has been used on a launch vehicle that possesses a high thrust-to-weight ratio, can operate over a wide range of Mach numbers, and perform with a high I_{sp}. Airbreathing propulsion can operate with high I_{sp}, but different propulsive devices are needed for various Mach number regimes. Gas turbines are ideal for Mach numbers up to Mach 3. Beyond that, Ramjets and Scramjet modes are needed for high supersonic and hypersonic flight. Air-breathing propulsion cannot function in vacuum conditions, preventing them from being used to put a vehicle into orbit. Rocket propulsion benefits from high thrust-to-weight ratios and the ability to operate at any encountered Mach number and continue to operate in the vacuum of space. This comes at the cost of low I_{sp}. The RBCC engine combines traits of both air-breathing and rocket propulsion to allow for a multi-mode propulsive device that can operate from launch until orbital insertion. During supersonic atmospheric flight, I_{sp} increases of up to 250% have been reported. In rocket-only mode, the mixing duct can act as a high area-ratio nozzle to expand exhaust gases and improve I_{sp} in a vacuum environment. Daines et al. [9] published a review of various RBCC engines when used in Earth-to-Orbit applications. In this review, the role filled by RBCC engines is first established.

The technical challenges begin with airframe integration. The efficiency of any air breathing engine is directly linked to the efficiency of the inlet and how that air is ingested into the engine. Great attention must be given to ensure the vehicle design is well matched and integrated to the RBCC engine. Next, the use of a fixed geometry inlet may be possible, but could limit the performance of the engine. Under the wide range of operating conditions encountered, the inlet will have to perform functions from subsonic flight to hypersonic- a great engineering challenge. Another technical obstacle identified in this review when operating in ejector mode is optimizing flow mixing without excessive mixing duct length. The optimal mixing duct $\frac{L}{D}$ is 8.5 for an RBCC engine with a central mounted, circular cross section rocket nozzle creates drag and weight penalties for the launch vehicle. Schemes such as clustering multiple engines together, annular or concentric nozzles, and mixer lobes have all been considered to decrease mixing duct length by increasing shear area between the primary and secondary flows.

Brevig [12] investigated the performance of a shrouded rocket in his study and compared its performance to a conventional launch vehicle powered by a chemical rocket. Brevig assumed the shrouded rocket would have complete and instantaneous combustion with no additional fuel for an afterburner being used. Also in the list of assumptions was that the primary flow entering the mixing duct with the secondary flow was perfectly expanded and fully mixed. Brevig stated that the assumption of complete mixing of the primary and secondary flows was one of the most significant to ensure maximum performance in ejector mode. Combustion analysis was also used in this model. The conclusions of this study were that the shrouded rocket offered significant improvements in specific impulse (I_{sp}) when compared to the reference rocket from Mach 1 to Mach 5 region. However, analysis of the shrouded rocket over the various trajectories revealed that the performance of the shrouded rocket was significantly impacted by the trajectory. Lower trajectories offered higher dynamic pressures on the inlet and mass flow rates of secondary flow. This led to the highest ratio of secondary to primary flow and thus, the greatest increase in I_{sp}. I_{sp} values over three times that of the reference rocket were predicted at supersonic flight velocities.

Foster et al. [7] performed a comprehensive study of promising RBCC engine configurations and their use on a new type of axisymmetric, fully-reusable launch vehicle for the Air Force Astronautics Laboratory. Five potential RBCC engine configurations and their potential use on SSTO launch vehicles were analyzed. The five configurations chosen were the Ejector Scramjet, Supercharged Ejector Scramjet, ScramLACE, Supercharged ScramLACE, and Recycled Supercharged ScramLACE. The five configurations were analyzed across the same 100 NM orbital mission profile with a 10,000 lbm payload. The benefits and disadvantages of each configuration were compared from a propulsion perspective. All configurations possessed some form of chemical rocket motor into which aspects of air breathing propulsion, such as mixing ducts, afterburners, or turbomachinery, were incorporated. The operating mode of the various RBCC engines were changed at different locations along the reference trajectory to take advantage of differences in the design of each engine configuration in order to maximize propulsive efficiency and thrust production. Each configuration was evaluated operating in the following modes- air-augmented, ramjet, scramjet, and rocket. This study concluded that all five configurations were capable of completing the mission performance objectives. However, recommendations were made to further study the ejector scramjet because it was able to achieve high specific impulse approaching 750 seconds while having the highest simplicity when compared to the other configurations.

2.2 Supersonic Ejectors

Gist et al. [15] analyzed a phenomenon known as Fabri-choking in a simulated 2D air-augmented rocket. Fabri-choking is a phenomenon where the primary flow is under-expanded when it enters the mixing duct. As a result, the primary flow expands through a Prandtl-Meyer expansion. This expansion causes the flowpath of the secondary flow to be constricted. If the correct conditions in the mixing duct exist, the secondary flow will become choked, limiting the amount of air that can be entrained into the mixing duct. The performance of the mixer can be evaluated by using the entrainment ratio Φ, shown in Equation 2.1.The entrainment ratio is the ratio of the mass flow rates of secondary flow to primary flow. Applying assumptions that the primary and secondary flows are choked and that the ratio of specific heats of the primary and secondary flow are the same, the equation used to predict the entrainment ratio is listed below.

$$\Phi = \frac{A_{1S} P_{0S}}{A_p^* P_{0p}} = \frac{w_s}{w_p} \tag{2.1}$$

A first-order inviscid model was used by Gist et al. [15] to attempt to predict the performance of the air-augmented rocket. Taking an experimental approach, a nitrogen cold gas thruster with a 2D test section was constructed such that ambient air could be entrained by the primary flow of the cold gas thruster and mixed in the test section. The test section equipped with static pressure ports, pitot probes, and thermocouples to capture data about the flow behavior inside the mixing duct. Comparison of the experimental results to the numerical model yielded that the model under-predicted the expansion of the primary plume and consequently, the limitations this put on the amount of secondary air that could be entrained into the mixing duct. Using the results from the experiment, empirical corrections were added to the numerical model in order to improve the model's accuracy. Models such as this can aid in preventing flow conditions like Fabri-choke which limit the performance of RBCC engines.

Etele et al. [11] studied the effects of various rocket exhaust configurations on the performance of RBCC engines. Their numerical solver used Favre averaged Navier-Stokes in combination with the Wilcox $k-\omega$ turbulence model. The solver was validated by using the test cases of Goebel and Dutton [16]. The two rocket nozzle configurations modeled were a single, centrally located rocket nozzle and a single, centrally located rocket nozzle with an annular nozzle working in conjunction. In addition, multiple cases were run that changed the distribution of the primary flow exiting from the centrally mounted nozzle and the annular nozzle. The results from this study revealed that the single, centrally located rocket nozzle configuration provided poor mixing. In the case with a single, centrally mounted nozzle, flow was not fully mixed until after a mixing duct $\frac{L}{D}$ of 10 was reached. A value consistent with $\frac{L}{D}$ values determined by empirical correlations in the literature [9]. The other configuration which utilized an annular nozzle in conjunction with the centrally located nozzle yielded significant improvements in flow mixing. At the end of the modelled mixing duct, the case with 75% of the flow being directed through the annular nozzle and 25% directed through the central nozzle yielded the highest compression ratio of entrained flow. Additionally, 95% of the exit plane of the mixing duct being occupied by the mixed flow region. This was a higher level of mixing seen than in any other condition or configuration tested.

Dijkstra et al. [10] conducted an experimental investigation to find the ideal mixing duct length for an ejector rocket and calculate the change in I_{sp} over the baseline rocket. An experimental setup was constructed which involved the use of an ethane gas generator to create the high temperature, high velocity exhaust gases of the primary flow. Air was allowed to be entrained from a hot air plenum chamber into the mixing duct through an inlet surrounding the primary nozzle. In order measure the baseline thrust of the rocket motor alone, the engine was fired with no entrained air. Next, the hot air plenum was opened to allow air to be entrained in a zero-velocity condition. Finally a case was run where hot air was forced into the mixing duct, simulating the forward flight of the ejector rocket.

Using thermocouples mounted in and upstream of the test section, it was concluded that the $\frac{L}{D}$ required for complete mixing of the primary and secondary flows to be 8.5. This was determined by comparing the wall and centerline temperatures and checking for when those temperatures became equal. At low Mach numbers, the increase in I_{sp} was only found to be 10-20 %. However, I_{sp} augmentation increased up to 230 % at high Mach numbers. This increase in I_{sp} at Mach numbers between 1 and 2 is particularly significant because this is a flight regime where ramjets cannot operate. The study determined ejector rockets to be a propulsion system that deserved more research and possible implementation on a launch vehicle.

Papamoschou [17] developed an analytical model capable of modeling a constant-area ejector where the exit flow remained not fully mixed. The primary and secondary flows within the mixing duct of the ejector were assumed quasi-one-dimensional. This meant that all variables and conditions of the primary and secondary varied only in the x-direction. To govern the dividing streamline between the two flows, the following equation was used.

$$\tau_* = K\frac{1}{2}(\rho_{\infty 1} + \rho_{\infty 2})(\Delta U)^2 \frac{(1+r)(1+\eta)}{2(1+r\eta)} f M_c \tag{2.2}$$

In this equation, K is a constant. $\rho_{\infty 1}$ and $\rho_{\infty 2}$ are the freestream densities of the primary and secondary flow. r is the ratio of primary to secondary flow and η is the ratio of primary to secondary velocities. M_c, or the convective Mach number, is used to quantify the compressibility of the shear layer. It is defined in the equation below.

$$M_c = \frac{\Delta U}{a_{\infty 1} + a_{\infty 2}} \tag{2.3}$$

The variables $a_{\infty 1}$ and $a_{\infty 2}$ are the respective speed of sound of the primary and secondary flows. Equation 2.4 is the function for convective Mach number which helped to characterize compressibility effects.

$$f(M_c) \simeq 0.25 - 0.75e^{-3M_c^2} \tag{2.4}$$

The change in convective Mach number was associated with compressibility effects limiting the growth rate of the shear layer, thus changing shear stress at the mixing layer.

Lastly the wall shear stress was determined by using the following equation.

$$\tau_w = c_f \frac{1}{2} \rho U^2 \tag{2.5}$$

The analytical model was computed in Fortran using these equations and applying the conservation equations for momentum and energy, along with additional parameters such as perfect gas assumptions, heat flux, and entropy change. The output of this model included area ratio effects on thrust augmentation, shear layer geometry, and ejector mixing duct effect on thrust augmentation. The equation below defines thrust augmentation.

$$\Phi = \frac{F_{ejector} - F_{jet}}{F_{jet}} \tag{2.6}$$

The experimental data of Krothapalli et al. [18] was used to verify the accuracy of the model. When compared to the experiment, there was agreement in the trends. Additionally, values such as peak pressure were within 15 % of experimental data. It was concluded that a quasi-one-dimensional model is capable of predicting two-stream ejector performance with reasonable accuracy. A finding of note was that the model predicted an increase in thrust production with increasing mixing duct length. However, as mixing duct length increased, performance returns decreased.

Dong et al. [6] conducted a numerical analysis of the flow field and mixing properties inside of an RBCC engine with a converging-diverging mixing duct operating in ejector mode. This publication was foundational for the current investigation as this is where the RBCC geometry, operating parameters, and model validation method originated from. Dong et al. created a two-dimensional model of a simplified RBCC engine mixing duct in the commercial CFD solver, ANSYS Fluent. By varying the geometry of the duct, the throat of the converging-diverging mixing duct could be changed to get different throat locations and contraction ratios. The accuracy of the model was verified through validation against data from a turbulent mixing experiment [16] and a supersonic inlet experiment [5].

After completion of the numerical modelling, it was found that a properly calculated increase in contraction ratio would enable higher levels of mixing within the duct by strengthening shocks that form as the primary and secondary flows interact. Also, a reduction in distance from the beginning of the mixing duct to the location of the throat resulted in a slightly higher growth rate of the mixing layer. A converging-diverging mixing duct yielded higher performance than a constant-area duct. It also resulted in higher total pressure recovery.

2.3 Cooling Methods for High-Speed Propulsive Applications

Ewan & Evensen [2] provide an overview of ablative cooling use in rocket combustion chambers. Ablatively cooling involves using a flame-resistant liner inside of a structural component which provides strength. As the rocket motor fires, the liner undergoes pyrolysis. This results in erosion of the liner and heat from the exhaust is carried away from the remaining liner and the structural shell underneath.

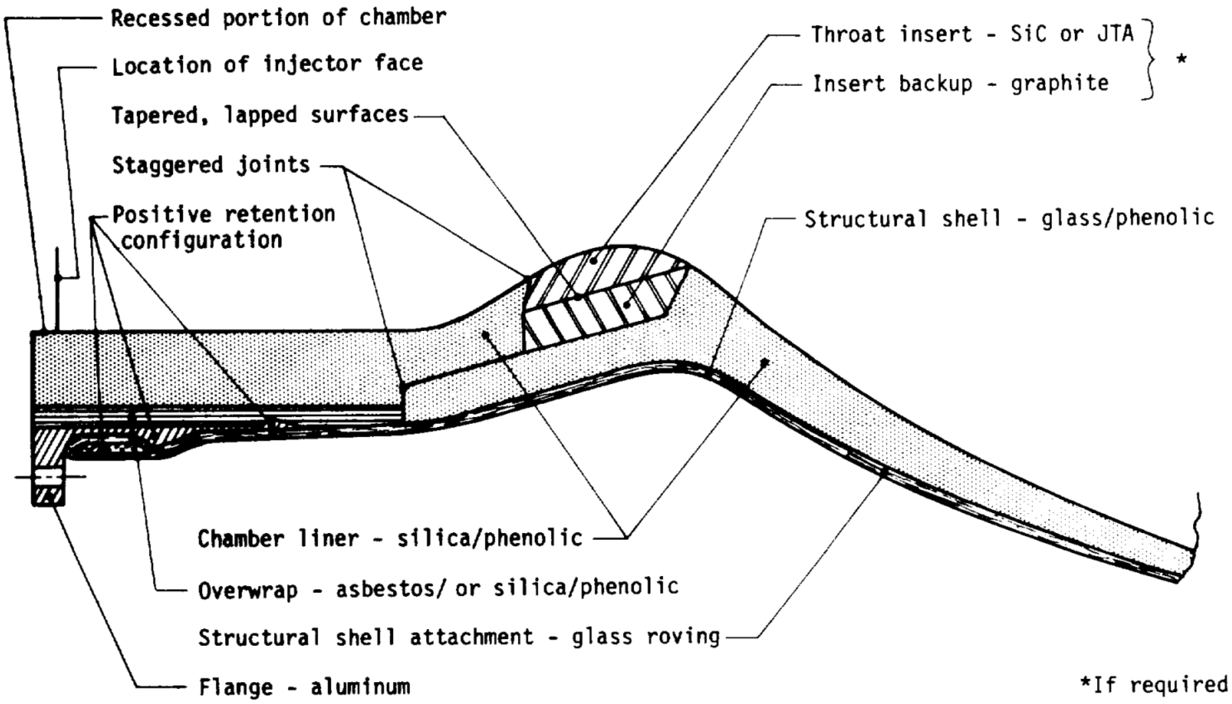

Figure 2.1 Diagram of components in an ablatively cooled nozzle [2]

Ablatively cooled structures have the advantage of being simple when compared to other cooling methods. Ablative chambers handle short duration operation and low throttle conditions well. Ablative chambers do have certain drawbacks. As the liner undergoes pyrolysis and erodes away, the geometry of the combustion chamber and nozzle change. This results in a change in engine performance as the geometry of the nozzle throat and walls change over time. Also, to address higher heat flux locations in the chamber, different materials may have to be used limit erosion rates. An example of this is the nozzle throat insert illustrated above in Figure 2.1. In addition, another limitation of ablatively cooled chambers is that the total burn time must limited to less than 10 minutes. This is due to the excessive amount of liner that would be required for long burn duration and the corresponding large change in internal geometry as that liner erodes away. The larger thickness of liner required for long burn times also adds weight to the structure. Care must be taken during design to use materials and material placement strategies that minimize weight, while still allowing for adequate cooling of the thrust chamber.

Huzel & Huang [3] list the advantages and disadvantages of regenerative cooling in the applications of cooling rocket thrust chambers and nozzles. Regeneratively cooled thrust chambers see applications in high-temperature flux environments. It involves pumping either a liquid fuel or oxidizer through small cooling channels within the walls of the thrust chamber. As the coolant passes through the cooling channels, heat is absorbed into the coolant. The preheated fuel or oxidizer is then is injected into the combustion chamber for thrust generation.

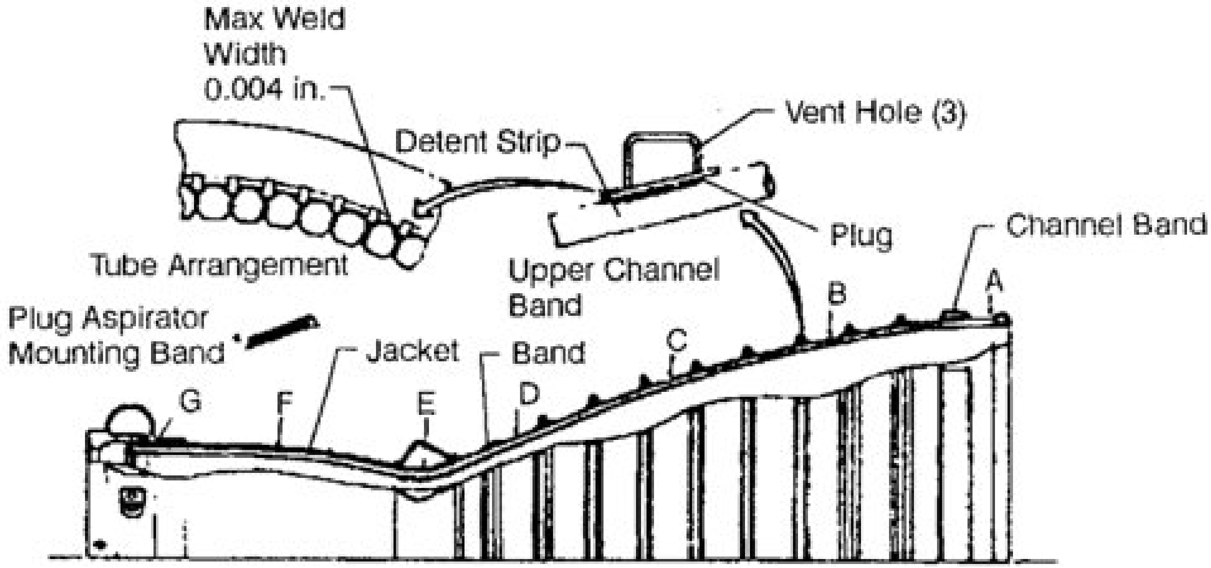

Figure 2.2 A depiction of cooling channels in a regenerative cooled thrust chamber [3].

Regenerative cooling has a few key advantages including no change in wall geometry over time, as seen with ablatively cooled chambers. Additionally, there is no limitation on burn time. So long as propellant is being fed to the engine, the regenerative cooling system will continue to function. The weight penalty is also less when compared to other methods. Regenerative cooling, however, limits throttling ability of the engine since throttling has a direct impact on flow rates of coolant through the cooling channels of the thrust chamber. Also, high pressure drops occur at high throttle settings and this additional pressure drop must be overcome by the propellant feed system. Great care must be exercised in the design of a regenerative cooled thrust chamber to ensure proper functionality of the system, structural integrity, and that scenarios such as coking and soot buildup in the cooling channels are avoided.

Terry & Caras [4] document the uses of film cooling in liquid propellant rocket engine nozzles. Having been implemented as far back as the German V-2 ballistic missile of WWII, gaseous and liquid film cooling were seen as an effective cooling technique in the emerging field of liquid rocket engines. Liquid rocket engines tended to favor liquid film cooing due to the additional onboard storage requirements posed by a gaseous cooling medium. Use of a liquid coolant also had the advantage of having a higher specific heats than many gases, resulting in higher film cooling performance.

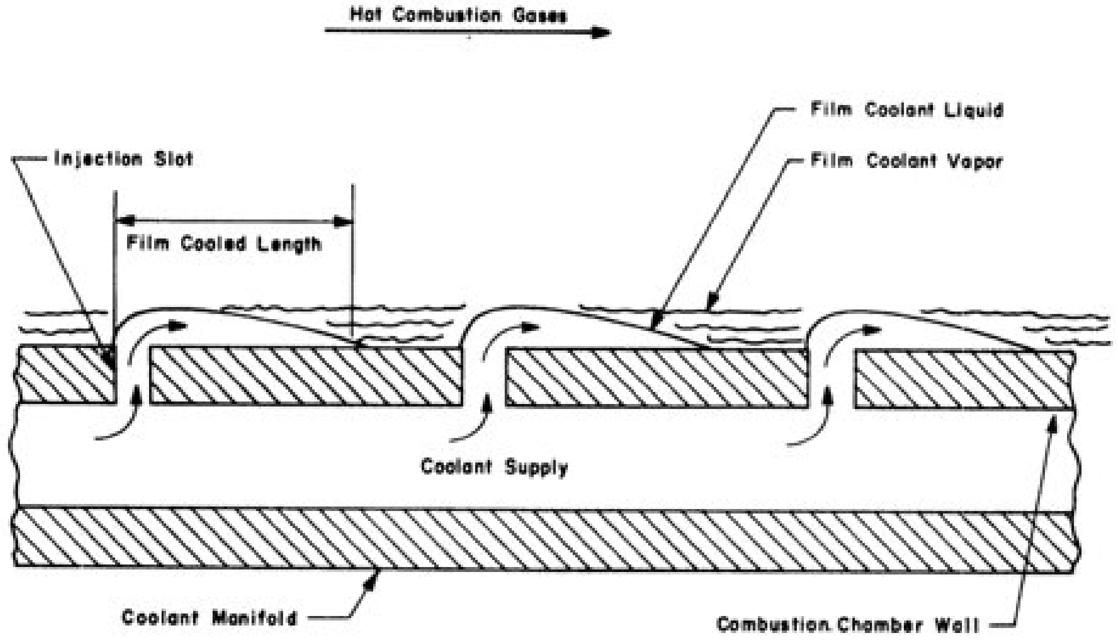

Figure 2.3 A simplified diagram of a film cooled combustion chamber [4]

Film cooling is noted to have several major advantages over other cooling methods. First, film cooling does not have the same limitations on total cooling capacity that regenerative cooled nozzles have. Also, there is no time limit when film cooling is used like in ablative cooling. Ablative liners can only provide thermal protection to the underlying structure for a finite amount of time before the ablative wall erodes away. Unfortunately, film cooling does have one major drawback. The coolant must be stored onboard in addition to the propellant for the engine, reducing the payload capacity of the rocket. If a fuel is used for film cooling, this could result in a change in oxidizer to fuel ratio in the thrust chamber and cause I_{sp} losses.

Schuchkin et al. [19] used a CFD solver to analyze the fluid dynamics and heat transfer properties of film cooling through porous slots in supersonic duct flows, and compared the solution to experimental results. The model used the Navier-Stokes equations with different forms of the $k - \varepsilon$ turbulence model in order to model the flow field characteristics and performance of the film cooling system. The model utilized a finite-volume, pressure based solver with a second-order, central differencing scheme. An adiabatic wall condition was used in the model on the film-cooled surface.

From this study, it was found that the Navier-Stokes with $k - \varepsilon$ turbulence model predicted the streamlines near the wall reasonably well. On the other hand, the pressure and adiabatic wall temperatures did not yield solutions that accurately recreated the experimental data.

Hombsch et al. [20] conducted experiments of supersonic film cooling with laminar and turbulent boundary layers. With the application of film cooling liquid propellant rocket engines in mind, the goal of this study was to investigate how film cooling performance, characterized by film cooling efficiency, is affected by changing film cooling injection angles and mass flow rates. Additionally, different coolant gases were tested to measure the change in film cooling efficiency. Flow was passed over an inclined flat plate and two ramp wedge in with different injection schemes across Mach numbers ranging from 1.5 to 8.3. Sandpaper could also be attached to the leading edge of the wedge in order to initiate a transition to a turbulent boundary layer. Following the completion of this experiment, it was found that increasing the mass flow rate of coolant increased film cooling efficiency. Additionally, this increase in performance was more noticeable in laminar boundary layers rather than turbulent boundary layers. Operating cases with higher Reynolds numbers also yielded higher film cooling efficiency due to thin boundary layers. It was also found that tangential injection of coolant performed better than angled slots or blowing holes. As noted by this study, one of the most important parameters to maximize film cooling efficiency is the density of the coolant. Higher density coolants performed best in this experiment.

2.4 Thesis Objectives

The primary objectives of this study are to use STAR CCM+ to model the thermal trends within a constant-area, two-dimensional RBCC engine mixing duct. The changes in these trends are to be observed after varying the L/D of the mixing duct as well as modelling four distinct phases of flight along a reference trajectory. The goal is to determine if certain mixing duct L/D values or phases of flight increase thermal stresses on the mixing duct. Lastly, this study aims to analyze whether the entrained secondary flow of air is capable of pseudo-film cooling the mixing duct walls under these various operating conditions.

3 Methodology

This section will focus on how the internal flow and thermal conditions of an RBCC engine's mixing duct were modelled using computational fluid dynamics (CFD) in Simcenter STAR CCM+ 17.04.008. STAR CCM+ is a commercially available CFD software produced by Siemens and sees use in the automotive and aerospace industries. It features the ability to construct geometries, generate meshes, run CFD computations, and conduct data post-processing in one integrated software package [21].

3.1 Computational Fluid Dynamics

Computational Fluid Dynamics (CFD) is an application of numerical methods and analysis to obtain an approximate solution to fluid flow and heat transfer problems [22]. CFD allows for very detailed views of the thermal and fluid flow behaviors within and around a body and cannot be easily replicated by experimentation or theoretical approaches. Various schemes and numerical models have been developed in CFD to simulate or model the fluid flow and heat transfer behaviors [22].

3.2 Choosing CFD over Experimentation

The use of CFD was chosen over experimentation for a few key reasons. First, an experimental rig that can accurately measure temperature, heat flux, and pressure inside the duct of an RBCC would be costly and perhaps only find use with this one application. It would also be complex to design a testing rig that can accurately vary entrained air velocity, temperature, and pressure to simulate different phases of flight. Simultaneously, some form of vacuum chamber would have to be fitted aft of the mixing duct in order to simulate the proper back pressure in different phases of flight. Additionally, at the time of publishing, the Embry-Riddle Daytona Beach Campus does not have the facilities to test experimental chemical rocket propulsion. Solid propellant rocket motors would have been selected for use in this experimental rig due to their simplicity and cost effectiveness. Despite the high consistency of commercially available high-power solid rocket motors, small deviations in thrust curve can occur of motors of the same class. These small differences from motor to motor would potentially have an effect on the result of the experimental trials.

CFD overcomes many of these obstacles. It allows for the altering of boundary conditions to accurately simulate different phases of flight. Within the CAD program in STAR CCM+, the geometry of the mixing duct can be quickly manipulated to allow for multiple mixing duct L/D values to be tested in quick succession. Performing this study in CFD yields another key benefit. Hobby-grade solid propellant rocket motors fire for relatively short burn times, under 10 seconds, with peaks and dips in thrust generation. A CFD model can be run in steady state conditions with steady thrust levels to allow for analysis of the internal flow field and thermal conditions to be analyzed at a specific operating condition. This allows for transient effects to not have to be considered during data analysis.

3.3 CFD Model Reference Geometry

The reference geometry being modeled in this study is the two-dimensional mixing duct used by Dong et. al [6]. This geometry in Figure 3.1 represents a simplified and generic interior of a RBCC engine's mixing duct.

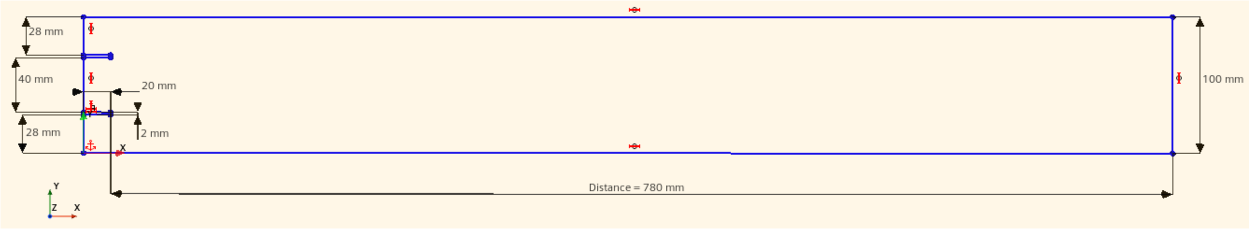

Figure 3.1 Mixing duct geometry from Dong et al. with dimensions

Table 3.1 Mixing duct dimensions [6]

Feature	Length (mm)
Distance from Splitter Tip to Exit	780
Total Height	100
Primary Inlet Height	40
Secondary Inlet Height	28
Splitter Thickness	2

Starting on the left side of the geometry, there are three inlets through which air enters the mixing duct. The inlet on the centerline of the mixing duct is called the primary inlet. The primary inlet is 40mm in height and represents the exit plane of a chemical rocket engine's nozzle. It is here the rocket exhaust will enter the mixing duct. Above and below the primary inlet are the upper and lower secondary inlets, each with a height of 28mm. The two secondary inlets are where the air from the atmosphere will enter the mixing duct. Separating the three inlets are two splitters. Each splitter has a thickness of 2mm and serve to separate the flows until entering the mixing duct. The total height of the geometry is 100mm. The top and bottom of the geometry are the walls of the mixing duct. The walls have a length of 780mm from the end of the splitter plates to the outlet on the right [6].

3.4 Boundary and Operating Conditions

The boundaries for the primary and secondary inlets were set to stagnation inlets and the boundary for the outlet of the mixing duct was set as a pressure outlet. The splitter plates and walls on the upper and lower side of the mixing duct were set as adiabatic wall boundary condition with no-slip condition applied.

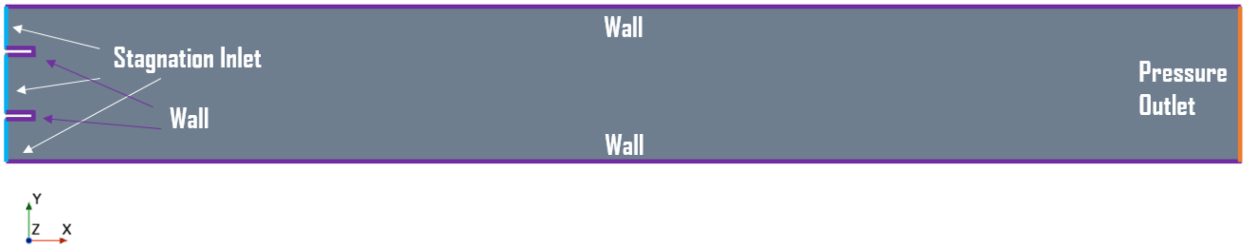

Figure 3.2 Geometry of air-augmented rocket from Dong et al. with boundary conditions

The stagnation inlet boundaries are color coded blue in the figure above. No-slip walls are color coded purple and the pressure outlet at the exit of the mixing duct is colored orange.

In this baseline case, it is important to note that both the primary and secondary flow are supersonic and the primary flow of the modeled rocket exhaust is perfectly expanded.

This is a condition that will happen only once in the ascent of a launch vehicle.

3.5 Numerical Scheme and Turbulence Modeling

An important part of CFD and numerical heat transfer modelling is the selection of the numerical models used to predict flow-field and thermal behaviors. The selection of the appropriate numerical models will result in accurate predictions in the interactions of the primary and secondary flows and thus, accurately model the flow-field conditions near the mixing duct walls, where heat transfer will occur.

Some CFD algorithms attempt to simulate the actual flow field with methods such as Direct Numerical Simulation (DNS) and Large Eddy Simulations (LES). DES involves solving the unmodified Navier-Stokes equations and provides for the highest level of simulation accuracy [22]. LES calculates the mean flow as well as large and medium scale flow phenomenon while sacrificing small-scale fluctuations to lower computational cost when compared to DNS [22]. While methods such as DNS and LES can result in some of the most accurate results, this is a computationally expensive approach that produces large grid sizes. The high amount of computing power required to handle large grids can be a major limitation to researchers with smaller computing capabilities. Additionally for a preliminary study such as this one, the use of a computationally expensive method is not warranted.

Methods such as Reynolds Averaged Navier-Stokes (RANS) aim to solve the high computational cost issues of DNS and LES. RANS models fluid flow by applying averaging operations to the Navier-Stokes equations. Through the use of Reynolds stresses and Turbulent Kinetic Energy with the corresponding transport equations, it is possible for RANS to model turbulent oscillations on local and mean flow levels [22]. The problem with the created transport equations is that the averaged flow variables used cannot lead to a solvable system of equations [22]. More unknowns exist than equations due to the addition of higher-order terms. To solve this, RANS modeling requires a closure model. The closure model is based on experimental and numerical data and flow assumptions that are made of the nature of turbulence [22]. The closure model adds more equations to the system.

The closure model used in this study was Menter's $k - \omega$ shear stress transport (SST) turbulence model with a 2^{nd} order convection scheme. $k - \omega$ SST is a two-equation closure model that uses turbulent kinetic energy (k) and specific dissipation rate ω to determine turbulent eddy viscosity [21]. This model was chosen because of the success seen in its use by Dong et al., where the $k - \omega$ SST model performed well in capturing the complex shock structures mixing behaviors within the mixing duct [6]. The $k - \omega$ SST turbulence model corrects some of the drawbacks of the original $k - \omega$ model, by using a blending function to combine aspects of $k - \varepsilon$ in the flow farfield with $k - \omega$ along wall boundaries [21] The result is accurate modeling of the flow field throughout the domain.

Further, the model was run as steady-state with an implicit, 2^{nd} -order upwind scheme for the coupled flow equations. RANS would be solved using the ideal gas model. For evaluating inviscid fluxes, a Roe Flux Difference Splitting scheme was used on the convective term. Lastly, an automatic Courant-Friedrichs-Lewy (CFL) control method was employed. This method allowed for the CFL number to be adjusted based on the performance of the Algebraic MultiGrid (AMG) solver in real time. Thus during the course of the calculation, time-step size was adjusted while maintaining accuracy.

By sacrificing some of the accuracy of DNS and LES, RANS allows for flow modelling to be done at a much lower computational cost [22]. This tradeoff of higher modelling error for lower computational expense is justified in an engineering context because the accuracy of the model is still high enough to provide detailed flow predictions which can be used to make informed engineering decisions.

3.6 Meshing for Baseline Case

The mesh used in baseline mixing duct geometry is shown in Figure 3.3. To produce this grid, a polygonal cell mesher was use generate cells in the domain. The base cell size that was utilized was 1mm.

Figure 3.3 Mesh used for the 2-D baseline mixing duct case

Along the splitter plates and the walls of the mixing duct, a prism layer mesher was used to ensure detailed modelling of the boundary layer and heat transfer along the mixing duct walls. As shown in Figure 3.4 below, the total thickness of the prism layer is 1.25mm. It has 40 total layers with a prism growth rate of 1.2 and a stretching factor of 1.1.

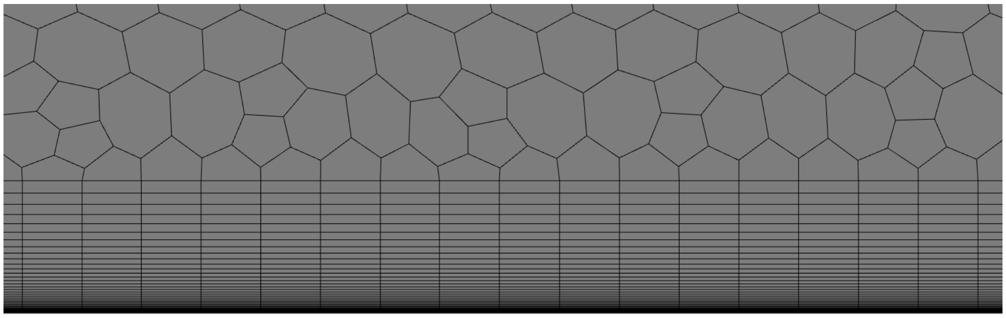

Figure 3.4 Prism layers growing off the mixing duct wall

Ensuring the proper total thickness of the prism layer and the total number of prism layers is essential to obtain a y+ value of less than 1. A low y+ wall treatment model was applied to all walls in the domain. Achieving the proper y+ value along the wall will allow for the proper resolution of the viscous sublayer and a more accurate temperature and heat transfer gradients to be computed [21].

To enable higher fidelity modeling of the mixing regions off of the upper and lower splitter plates, the wake refinement tool was used. With a target cell size of 0.5mm and a cell growth rate of 1.3, the wake refinement criteria was applied to the domain downstream of the splitter tips at a spread angle of 3°.

Figure 3.5 Wake refinement propagating off the splitter plate tips

Wake refinement was applied on a total length of 1,150mm downstream of the splitter tips. This allows for the growing mixing region to be fully captured more accurately and modeled without wasting computing power by applying the 0.5mm grid size to the entire mesh. It resulted in a total number of 458,445 cells in this mesh.

3.7 Mesh Independence Study

A mesh independence study determines the minimum required mesh size for obtaining solutions to the desired accuracy such that the solution no longer significantly varies with mesh size. The mesh independence study was conducted by adjusting the base cell size in STAR CCM+. This resulted in an increase or decrease in the total number of cells in the mesh. The mesh size and corresponding base cell size are shown in the table below.

Using the grid and base cell sizes listed above, the average pressure across the upper wall of the mixing duct were extracted from each model. This parameter was selected because the average pressure value along the upper wall captures overall flow trends such as boundary layer and shock interactions with the wall. The average pressure should only change as a higher cell count will help better resolve these flow phenomenon interaction with the wall.

Table 3.2 Mesh sizes with corresponding base cell size and upper wall average pressure

Mesh Size	Base Cell Size (mm)	Upper Wall Average Pressure (kPa)
350,534	1.18	42,451.3
401,309	1.09	42,177.1
458,445	1	41,846.5
507,049	0.95	41,608.6
556,005	0.91	41,458.4
600,666	0.859	41,177.4
649,729	0.819	40,968.4

The average upper wall pressure at different mesh sizes was plotted to see how the solution varied with mesh size in the figure below.

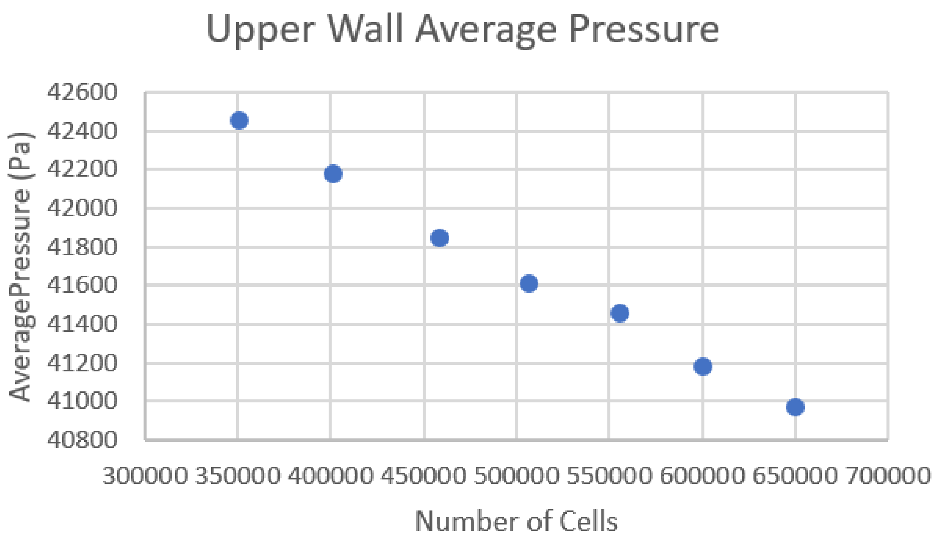

Figure 3.6 Change in average pressure along upper wall plotted against mesh size

The mesh independence study found a solution percent different of 3.62% across the entire range of evaluated meshes. With a percent difference of 0.57% from 458,445 cells to 507,049 cells, a grid size of 458,445 cells was chosen with a target cell size of 1mm. Since this is an initial study focused on identifying thermal trends and behaviors, it was deemed acceptable to use the smaller grid since the change in solution is only about 0.5% from this mesh to the next finer one. Additionally, the selection of a mesh with a lower total number ofcells was done for better computational speed. In all, the mesh size chosen provided a balance between accuracy and computational time.

3.8 CFD Model Validation

In order for a CFD model to be considered working correctly, the results of the model must be compared to experimental data to ensure that the predictions of the model are accurate and agreement exists between the model and the experiment. This is referred to as the CFD validation process. Only after a CFD model is validated can the predictions of the model be used to make engineering decisions.

3.9 Validation of Shock Waves and Wall Pressure Distribution

Following the method of Dong et. Al. [6], two experiments were used to validate the numerical model of the RBCC mixing duct in STAR-CCM+. The first experiment used for model validation was the investigation of internal compression of a hypersonic intake performed by Herrmann and Koschel [5]. This experiment featured the testing of a two-dimensional supersonic inlet in a supersonic wind tunnel. The inlet geometry and dimensions are depicted in the Figure 3.7.

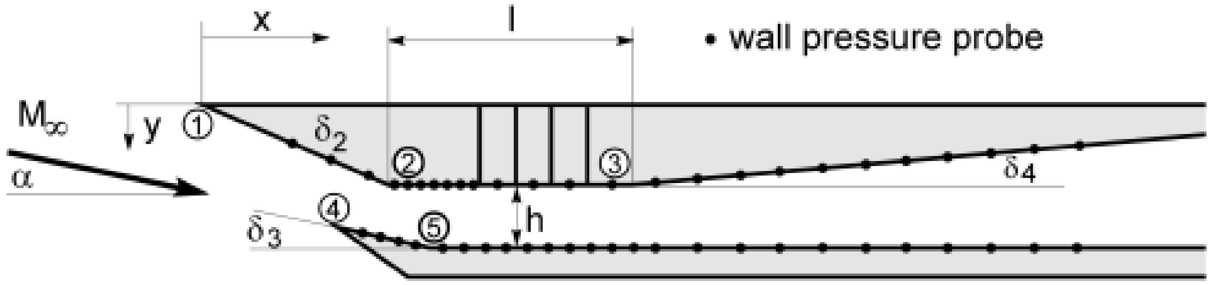

Figure 3.7 Inlet geometry [5]

The inlet features a ramp on the upper surface and a lower lip. These lead to a constant-height isolator before diverging towards the end of the inlet. An optical access window located on the side of the inlet allowed for color-schlieren images to be taken that capture major flow phenomenon such as shocks, expansion waves, flow separation and reattachment, as well as the interaction of these phenomenon with the boundary layer [5]. Listed below is a table of the dimensions of the inlet used by Herrmann and Koshel.

Table 3.3 Main inlet dimensions [5]

Feature	Dimension
Inner width of intake	52mm
Channel height	15mm
Total length	400mm
Angle of Freestream Flow	10°
Ramp Angle	21.5°
Lip Angle	9.5°
Isolator Divergence Angle	5°

The operating conditions used in the CFD validation model come from Herrmann and Koschel's Mach 2.5 testing conditions with zero throttling [5]. Test conditions are provided in the table below.

Table 3.4 Test conditions used for inlet experiment [5]

M	T_t (K)	P_t (kPa)	Re ($\frac{1}{m}$)
2.5	295	560	$5.07 * 10^6$

Comparing a density contour plot from the CFD model in STAR CCM+ to the color-schlieren images of Herrmann and Koschel allows for a qualitative assessment of the proper functionality of the CFD model. If the density contour plot and color-schlieren images show a reasonable resemblance, it can be concluded that the appropriate numerical models and grid have been utilized to achieve flow results that agree with real-world physical behavior. Density contour plots that are consistent with the color-schlieren images of Herrmann and Koschel indicate that the model is capable of accurately modelling the complex shock interactions and compressibility effects within the inlet.

In addition to the qualitative validation method mentioned previously, a quantitative comparison to the intake experiment was made by comparing wall pressure distribution. Comparing the experimental to wall pressure distribution to that of the model indicates whether the model is able to properly predict behaviors along the wall and in the boundary layer.

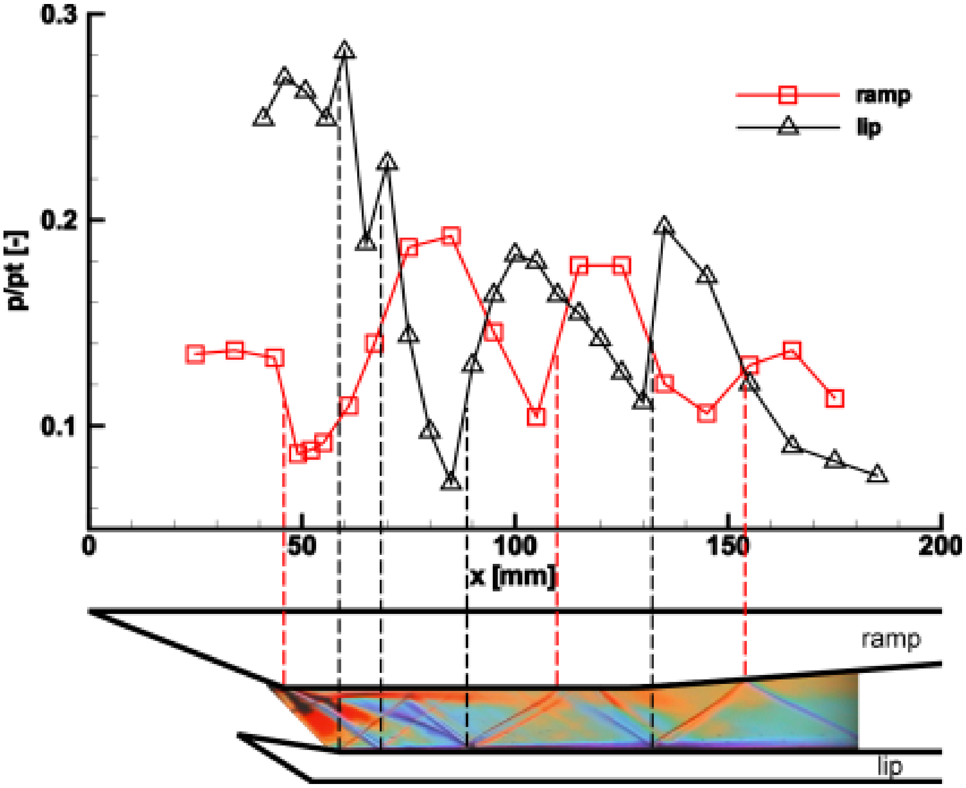

Figure 3.8 Wall pressure distribution and color-Schlieren image [5]

The wall pressure distributions aligned with the color-Schlieren image from Herrmann and Koschel [5] are shown above.

The model in STAR CCM+ shows strong correlation to the color-Schlieren image from Herrmann and Koschel's experiment. The shocks coming off of the upper ramp and the lower lip strike the inside of the inlet and reflect off of the upper and lower walls, resulting in a shock train that propagates down the length of the inlet. Another flow feature that the

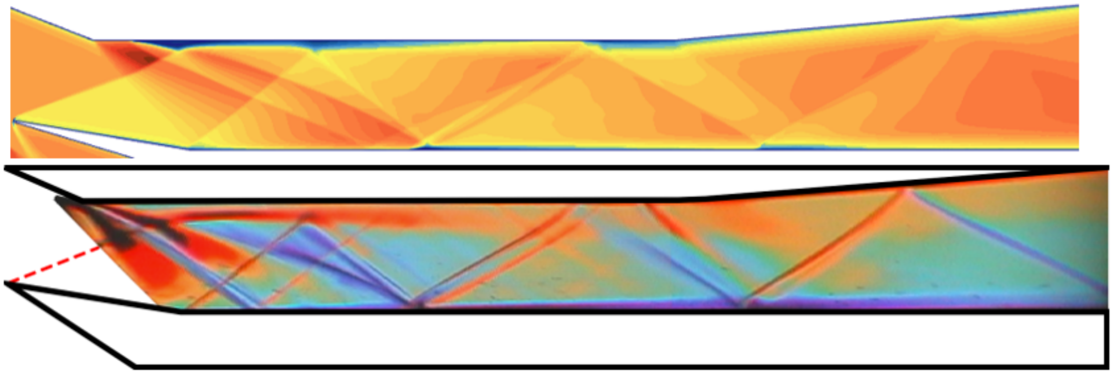

Figure 3.9 Mach contour plot showing modelled shock train inside inlet STAR CCM+ above and a color-Schlieren image from Herrmann and Koschel experiment [5]

model captures is the separation bubble that was identified by Herrmann and Koschel right after the upper ramp joins the upper wall.

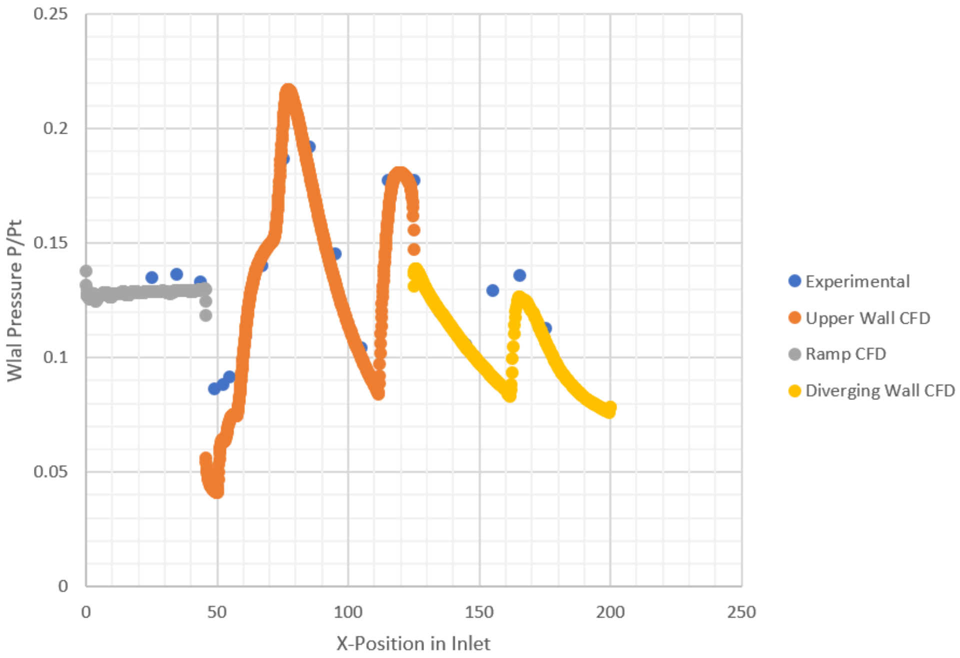

Figure 3.10 Experimental and CFD wall pressure distribution for the ramp and upper wall

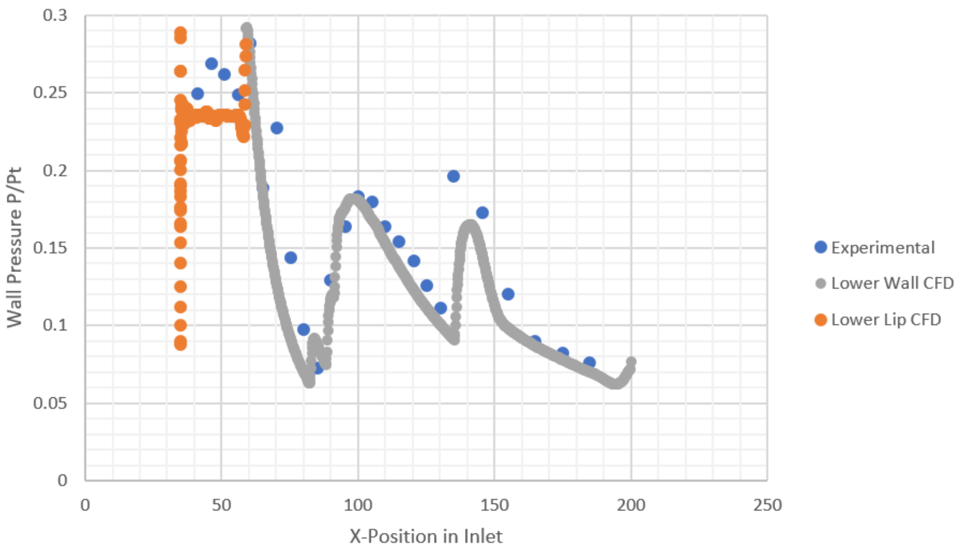

Figure 3.11 Experimental and CFD wall pressure distribution for the lip and lower wall

As seen in the figures above, the CFD model demonstrates trends that closely mimic the wall pressure distributions collected experimentally by Herrmann and Koschel. The model can be considered validated due to its ability to capture these trends in wall pressure.

The ability to match pressure distribution accurately along the wall is vital to the eventual modelling of thermal conditions along the wall of the RBCC engine's mixing duct. Flow phenomenon occurring in the middle of the mixing duct such as mixing and shocks will propagate outward towards the duct walls. The shocks reflected from the mixing duct wall will affect heat transfer and temperature distribution as they interact with the boundary layer.

3.10 Validation of Compressible Mixing Layers

The second experiment used for model validation was Goebel and Dutton's experimental study of compressible turbulent mixing layers. Goebel and Dutton's experiment was conducted to investigate the mixing behavior and flow development of two-dimensional high-speed, compressible flows [16].

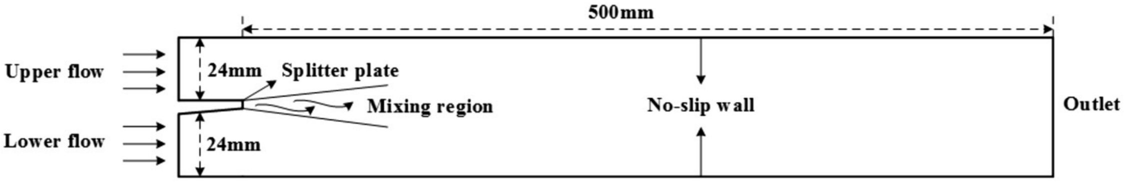

Figure 3.12 Geometry of Goebel and Dutton's mixing section [6]

In this experiment, a primary and secondary stream of differing Mach number and velocity were fed into the test section. Initially separated by a thin splitter plate, the two streams were brought together in a common mixing zone to create a compressible mixing layer. Passing downstream of the splitter, turbulent mixing that results from the different velocities of the primary and secondary flows produces a velocity gradient over the height of the test section.

Goebel and Dutton's experiment was modeled using the Case 4 operating conditions shown below.

Table 3.5 Case 4 operating conditions

Operating Condition	Flow 1	Flow 2
M	2.35	0.3
T_t (K)	360	290
U ($\frac{m}{s}$)	616	100
P (kPa)	36	36

After modelling Goebel and Dutton's experiment in STAR CCM+, the solution of the model yielded a mean streamwise velocity profile that was plotted against the experimental data of Goebel and Dutton.

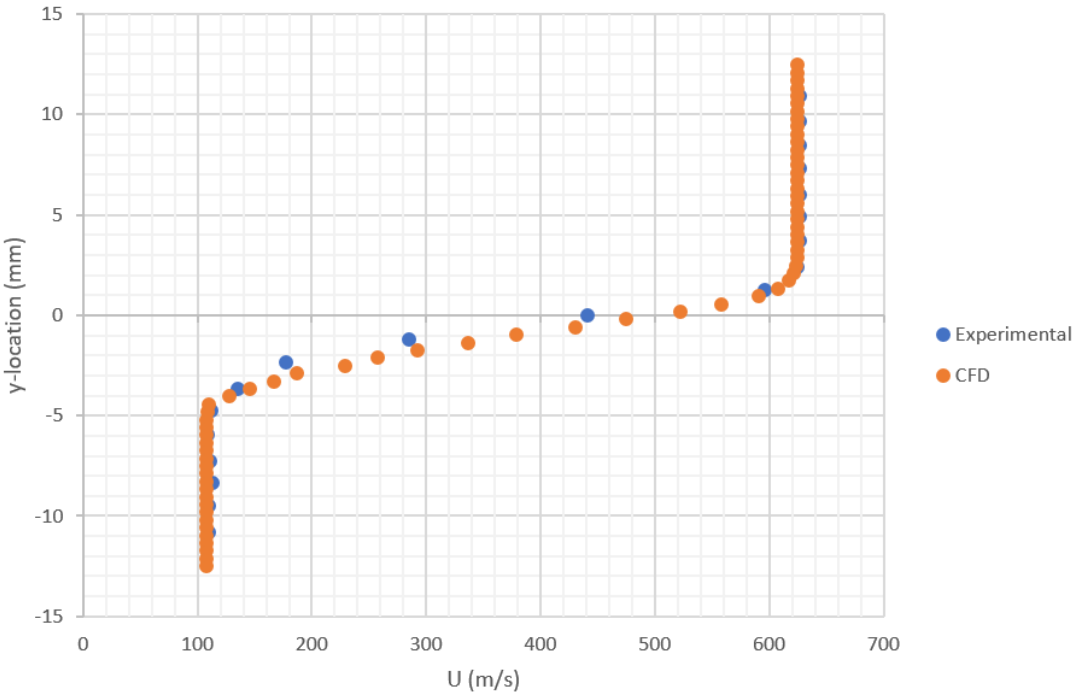

Figure 3.13 Experimental and CFD mean velocity profiles for case 4 at x = 50mm

As shown in Figure 3.13, the mean streamwise velocity modeled in CFD shows a strong resemblance to the experimental data from Goebel and Dutton. This demonstrates that the model has the capability to accurately predict the mixing behavior of two compressible flows in such a way that reflects true physical behavior. On the basis of this validation of compressible flow mixing behaviors, realistic modelling of the mixing of the primary and secondary flows within the mixing duct of the RBCC engine can be expected.

The accurate modeling of turbulent mixing behavior inside an RBCC engine mixing duct is essential to see how the hot gases of the primary flow mix with the secondary flow. Depending on how the mixing layer develops, it could have implications on the heating profile and the temperature and heat transfer coefficient on the mixing duct walls.

4 Data Reduction

4.1 Flow Analysis

To begin flow analysis, it is important to understand the ideal gas law, shown below in Equation 4.1. In this equation, P is the static pressure, ρ is the fluid density, R is the gas constant, and T is the static temperature.

$$P = \rho R T \tag{4.1}$$

This equation of state governs the relationship between pressure, density,and temperature in a gas. Under the ideal gas law, a few assumptions are made: the path of molecules shall be random and inter-molecular forces are negligible [23].

In addition to the ideal gas law, an important quantity that was measured is the mass flow rate shown below in Equation 4.2. Mass flow rate is a measurement of how much mass of gas passes through a given area per unit time.

$$\dot{m} = \rho v A \tag{4.2}$$

Knowing the mass flow rate of air is vital for quantifying how much air the secondary flow is entrained into the mixing duct.

Another important metric for analyzing the flow is called the Reynolds number (Re). Reynolds number is a ratio of inertial to viscous forces in the flow [23].

$$Re = \frac{\rho_\infty V_\infty c}{\mu_\infty} \tag{4.3}$$

In this equation, ρ_∞ is the freestream density of the flow, v_∞ is the freestream velocity, μ_∞ is the dynamic viscosity of the fluid, and c is the characteristic length. Flows with low Reynolds numbers are laminar. Flows with high Reynolds numbers, such as those in this study, are turbulent and inertial forces dominate the flow.

Next, it was necessary to calculate the speed of sound. As described in Equation 4.4, a is the speed of sound, γ is the ratio of specific heats, R is the gas constant, and T is the static temperature of air.

$$a = \sqrt{\gamma R T} \tag{4.4}$$

Since γ and R are specific to air, it is observed that the local speed of sound in air varies based on changes in temperature. The calculation of speed of sound used to determine the Mach number of the flow, is discussed next.

Mach number is a ratio of flow velocity to the speed of sound [23]. Shown below in Equation 4.5.

$$M = \frac{v}{a} \tag{4.5}$$

Mach number is a useful parameter to characterize compressibility effects at different flight regimes. For flows with Mach numbers of $M < 0.3$ the flow is considered subsonic and incompressible, thus density does not vary significantly. For Mach numbers ranging $0.8 \leq M \leq 1.2$, the flow is considered transonic. Lastly, supersonic flow is characterized when $M > 1$ in all locations [23].

In order to calculate inflow conditions from the selected phases of flight, isentropic relations were utilized. Equation 4.6 was used to determine the relationship between static and total pressure and 4.7 was used to determine the relationship between static and total temperature [23]. The isentropic relations assume that the process being undergone is both fully reversible and adiabatic. Many real flow phenomenon can be assumed to be isentropic, so the isentropic relations are an effective way of calculating flow conditions [23].

$$\frac{P}{P_0} = 1 + (\frac{\gamma - 1}{2} M^2)^{-\frac{\gamma}{\gamma - 1}} \tag{4.6}$$

$$\frac{T}{T_0} = 1 + (\frac{\gamma - 1}{2} M^2)^{-1} \tag{4.7}$$

In Equations 4.6, P is the static pressure, P_0 is the total pressure, γ is the ratio of specific heats ,and M is the Mach number. In Equations 4.7, T is the static pressure, T_0 is the total pressure, γ is the ratio of specific heats ,and M is the Mach number. By substituting γ, M, and P or T at a given flight condition, it was possible to calculate total pressure and temperature values which could then be implemented as inflow values in the CFD model.

4.2 Heat Transfer and Film Cooling

The study of thermal trends within the mixing duct requires an understanding of heat transfer. Heat can be transferred via three processes, conduction, convection, and radiation [24]. In this study, convection was the main heat transfer mode that was analyzed. Conduction was ignored as the walls of the mixing duct were set as adiabatic. Additionally, radiation was not investigated. Convection is the mode in which energy is transferred between a solid and a fluid. A higher flow rate of fluid results in a greater rate of heat transfer [24].

Film cooling involves the injection of a cooling fluid between a source of hot gas and a solid surface in order to insulate the surface and convect heat away from it. A parameter used to quantify the performance of film cooling is called adiabatic film cooling effectiveness [25]. The equation used for film cooling effectiveness is shown below 4.8.

$$\eta = \frac{T_{01} - T_{w,ad}}{T_{01} - T_{02}} \tag{4.8}$$

Here, T_{01} is the total temperature of the hot gas, $T_{w,ad}$ is the temperature of the adiabatic wall, and T_{02} is the total temperature of the coolant gas [25]. The closer the temperature of the adiabatic wall is to the coolant gas, the higher the film cooling effectiveness. This means that more heat is able to be removed from the adiabatic wall and transferred into the coolant gas.

Lastly, to characterize the amount of heat transfer along a wall, it is necessary to find the heat transfer coefficient.

$$h = \frac{\dot{Q}}{A_s(T_s - T_\infty)} \tag{4.9}$$

Shown above in 4.9, heat transfer coefficient is calculated by taking the heat transfer $\dot{Q}$, and dividing it by A_s multiplied by the difference of surface temperature T_s and the ambient temperature T_∞. Higher values of heat transfer coefficient result in a higher heat transfer rate on the contact area.

5 Testing Matrix

In this study, two different sets of parameters were modified to see their impact on the thermal trends and environment within the mixing duct of a generalized RBCC engine.

5.1 Mixing Duct Length Variation

For the first part of this study, the length-to-diameter ($\frac{L}{D}$) ratio of the mixing duct was incrementally increased while the inlet and outlet operating conditions remained constant. The existing literature for ejectors and RBCC engines has identified an ideal mixing duct length to diameter ratio of approximately 8.5 [10]. This ideal mixing duct $\frac{L}{D}$ of 8.5 is not absolute and engines have been tested with higher and lower values to satisfy different requirements. Table 5.1 below illustrates the different mixing duct lengths that were used in this study and the corresponding $\frac{L}{D}$ values for those mixing ducts.

Evaluating the RBCC engine with shorter and longer mixing ducts will allow for different mixing levels of rocket exhaust and air within the duct. These different levels of mixing have the potential to produce different temperature and heat transfer coefficient distributions along the wall. In addition to temperature and heat transfer coefficient distributions, film cooling effectiveness as introduced in the literature review will also be extracted from the

Table 5.1 Mixing duct lengths and corresponding L/D values

Duct Length (mm)	($\frac{L}{D}$)
400	4
500	5
600	6
700	7
780	7.8
800	8
900	9
1000	10
1100	11

model along the walls to evaluate the effectiveness of the entrained air in cooling the duct walls.

5.2 Varying Phase of Flight

In the second part of this study, the inlet and outlet conditions for the RBCC duct were varied to represent four phases of flight- launch, transonic, supersonic, and high-altitude. These phases of flight were extracted from the reference trajectory published in Air-Augmented Propulsion Concepts [7].

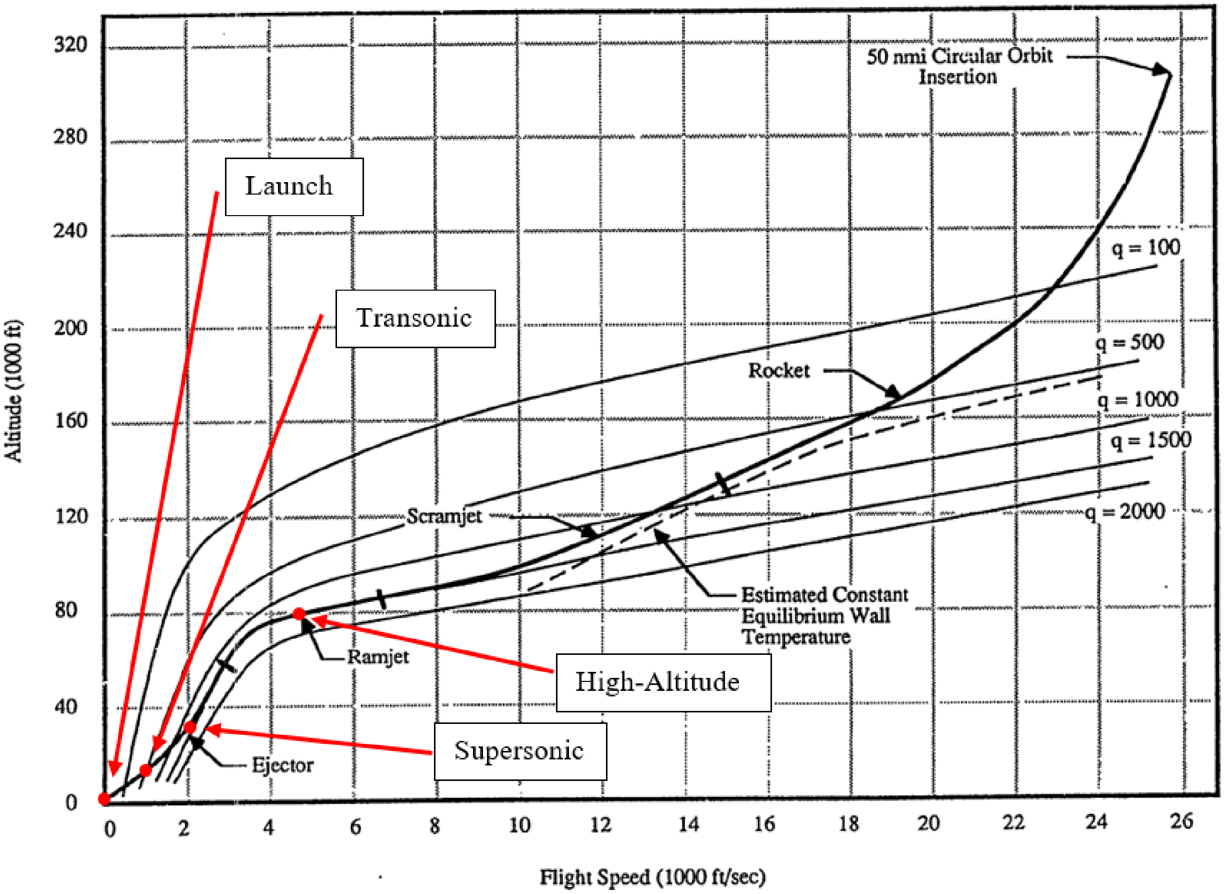

Figure 5.1 Reference trajectory for launch vehicle bolded with selected phases of flight highlighted in red [7]

From the reference trajectory of a traditional launch vehicle, shown in bold in Figure 5.1 above, flight conditions were extracted and used to create the inflow conditions for launch, transonic flight, supersonic flight, and high altitude flight. The flight conditions for the four selected phases of flight are listed in Table 5.2 below.

Table 5.2 Inflow conditions for secondary flow at different phases of flight

Phase of Flight	Altitude (ft)	Mach	U_∞ ($\frac{m}{s}$)	P (Pa)	T (K)
Launch	0	0	0	101,325	288.15
Transonic	13,854	0.944	305.4	59,894	260.7
Supersonic	30,000	2	609	30,149	228.8
High-Altitude	79,840	4.5	1,494.8	2,822.5	220.9

With a fixed geometry mixing duct and constant thrust level, the secondary flow velocity, pressure, temperature, and density will all vary as the simulated launch vehicle ascends on the reference trajectory. Unlike the baseline case which assumes a perfectly expanded flow, the four phases of flight selected will result in over- and under-expanded conditions where shocks will form in the primary flow. With the large change in flow conditions, there is a possibility that thermal trends within the mixing duct will also vary, with some phases of flight imparting higher thermal loads on the mixing duct walls than others.

6 Results and Discussion

In this study, mixing duct ($\frac{L}{D}$) ratio and phase of flight were varied in order to see their impact on the thermal stresses imparted on the walls of a constant-area, RBCC engine mixing duct. In total, nine different mixing duct lengths and four phases of flight were modeled. The effects of altering these parameters on the thermal conditions was investigated through the CFD modeling and the analysis of wall temperature, heat transfer coefficient, and local film cooling efficiency distribution on the mixing duct walls. Additionally, contour plots of temperature, Mach number, velocity, and pressure were used to visualize how flow phenomenon inside the mixing duct affected the aforementioned thermal parameters along the mixing duct walls.

6.1 Effects of Mixing Duct Length Variation

Changes in static temperature, heat transfer coefficient, and film cooling effectiveness, as a function of duct length, can be seen on Figures 6.1, 6.2, and 6.3. All solution data taken along the walls was extracted using a line probe which was located on the adiabatic wall boundary of the upper wall. With identical inflow conditions applied to both the upper and lower secondary inlets as well as the mixing duct geometry being symmetrical about the x-axis, the solution of flow and thermal parameters extracted from the upper wall can be considered identical to that of the lower wall.

On the previously mentioned figures, it was observed that the solutions for all mixing duct lengths overlay on top of one another. This suggests that the flow field and thermal conditions in a shortened mixing duct, such as the 0.4m case, share the same solution as what is present in the 0-0.4m x-location of a longer mixing duct, such as the 1.1m case.

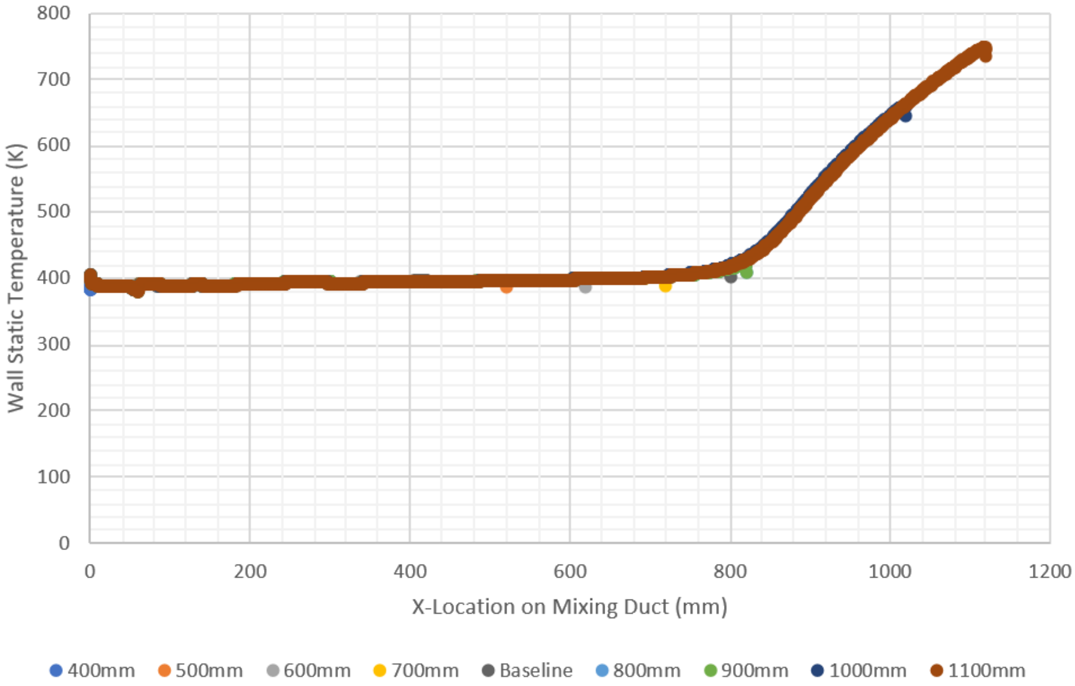

Figure 6.1 Static Wall Temperature vs. Length for Varying Mixing Duct Lengths

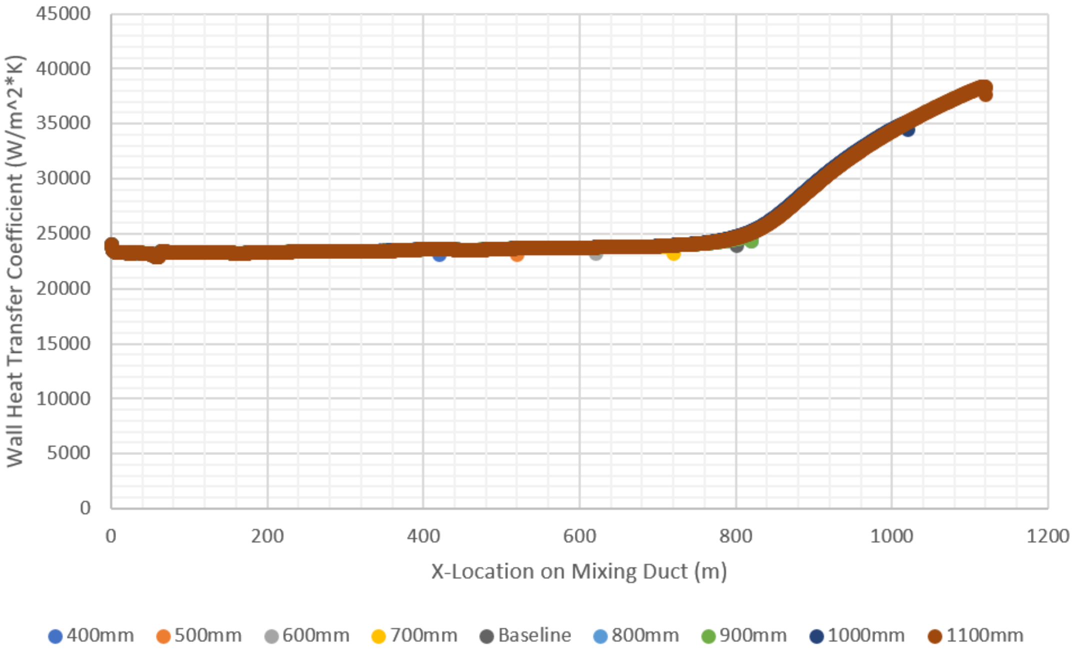

Figure 6.2 Wall Heat Transfer Coefficient Distribution vs Length for Varying Mixing Duct Lengths

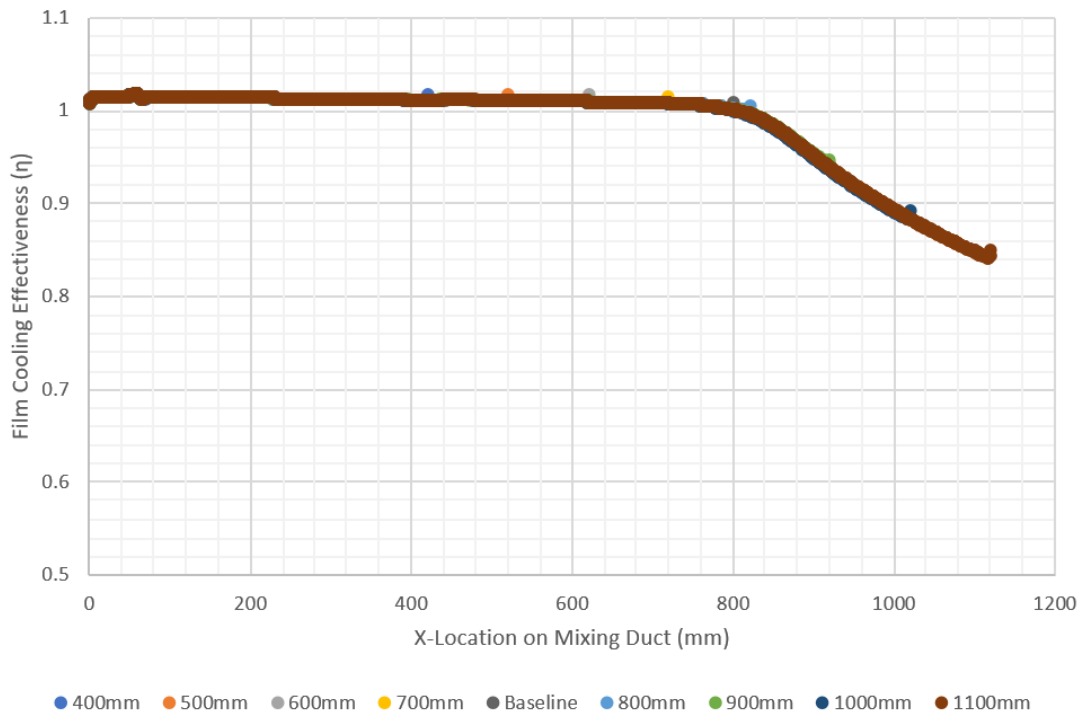

Figure 6.3 Wall Film Cooling Effectiveness vs Length for Varying Mixing Duct Lengths

Utilizing the flow conditions specified by Dong et al., the mixing ducts for all length cases were modeled with supersonic primary and secondary flows [6]. For duct lengths of up to approximately 700mm, the wall experienced a very small increase in wall temperature of 389K to 401K and heat transfer coefficient increase of 23,310 $\frac{W}{m^2K}$ to 24,000 $\frac{W}{m^2K}$. Simultaneously, the mixing duct wall was observed to have an almost constant film cooling effectiveness of $\eta = 1$ until a length of 700mm. These behaviors correspond with the contour plots of Figure 6.4, 6.5, and 6.6. The velocity contour plot points to a flow field consisting of two segregated flows at the end of the splitter plates that undergo turbulent mixing and the development of a mixing layer. This behavior is consistent with the results of Dong et al. [6]. Highlighted in Figure 6.6, there is a growth in an intermediate velocity region highlighted in green. At an x-location of approximately 700mm, the upper and lower mixing layers have grown to a point in which the primary flow gases begin interacting with the boundary layer along wall.

Returning to the film cooling effectiveness shown in Figure 6.3, it is important to address solutions for film cooling effectiveness which are greater than η =1. In a physical scenario, it is impossible to have a film cooling effectiveness of higher than η =1. In this study, values above η =1, with a maximum value of η =1.014, were observed. This is not physical behavior and cannot occur due to the laws of thermodynamics. The 0.014 disparity in film cooling effectiveness was attributed to numerical dissipation. The magnitude of this dissipation, however, can be considered negligible and will not have any significant effect on thermal trends observed inside the mixing duct in this preliminary study.

Contour plots displayed the mixing duct length variation section will be of the 1.1m long mixing duct ($\frac{L}{D}$ of 11) as it provides a representation of the CFD solutions for all mixing duct lengths modelled in this study.

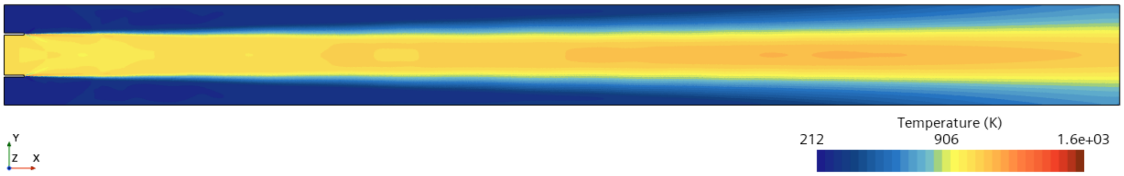

Figure 6.4 Temperature contour plot of 1,100mm long mixing duct

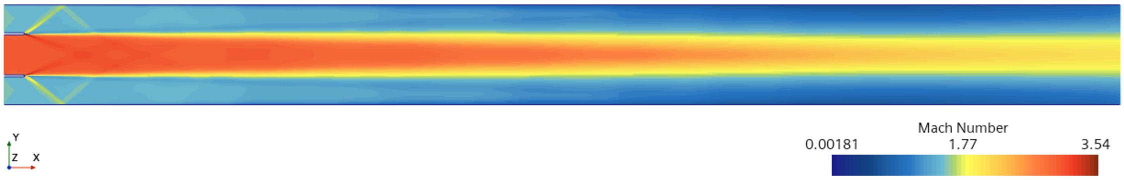

Figure 6.5 Mach contour plot of 1,100mm long mixing duct

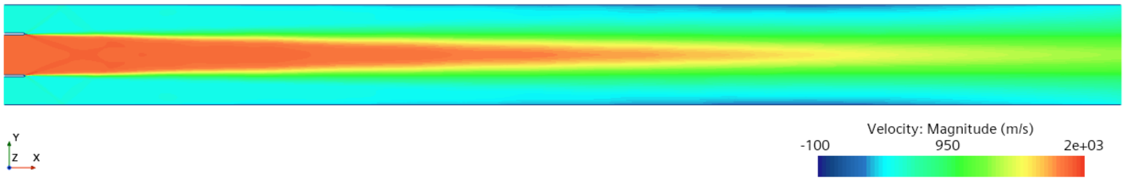

Figure 6.6 Velocity contour plot of 1,100mm long mixing duct

Film cooling effectiveness remains remarkably high until a mixing duct length of approximately 700mm is reached. The temperature contour plot in Figure 6.4 reveals that the air from the secondary inlets appears to provide an uninterrupted low temperature region along the mixing duct walls. It appears that the secondary flow insulates the walls from the high temperatures of the primary flow up until turbulent mixing begins to dominate the flow field close the mixing duct walls at distance of 700mm. This would suggest that under the operating conditions used in this study, the secondary flow into the mixing duct has a natural capacity to cool the mixing duct walls. Harnessing the cooling capacity of the secondary flow in future RBCC engine designs could allow for complex cooling systems such as ablative materials or generatively cooled structures to be avoided, reducing weight, complexity, and cost.

After an x-location of 700mm, the velocity contour plot of Figure 6.6 indicates high levels of mixing as indicated by the almost homogeneous velocity distribution from the lower to the upper wall of the mixing duct. As seen in Figures 6.1 and 6.2, once the mixing duct lengths exceeds 700mm, or the $\frac{L}{D}$ exceeds 7, the wall temperature and heat transfer coefficient began to grow rapidly. It is in this range of mixing duct lengths where Dijkstra et al. identified the ideal mixing duct $\frac{L}{D}$ to be 8.5, corresponding to a mixing duct length of 850mm length in this study, to be optimal for best mixing [10]. From this, a conflict of design interests was discovered. In order for higher mixing in the duct, as the literature suggests, an RBCC engine must feature a higher $\frac{L}{D}$ mixing duct. However, in order to reduce wall thermal loads, lower $\frac{L}{D}$ values should be used.

With the RBCC engine configuration modelled in this study of a constant-area mixing duct with a single rocket nozzle, reduction of the mixing length to an L/D of 7 or lower would be ideal to avoid the highest thermal loads inside the mixing duct. From a thermal management perspective, this configuration would result in the best possible cooling conditions to prevent excessive heating of the mixing duct.

6.2 Effects of Varying Phase of Flight

Using the baseline duct length of 780mm as modelled by Dong et al. described previously, a generalized two-dimensional model of a constant-area mixing duct was modelled under launch, transonic, supersonic, and high-altitude phases of flight. Each phase of flight selected from the reference trajectory presents a unique set of operating conditions which have the potential to create different flow mixing environments within the mixing duct. Varying the secondary flow velocity, pressure, Mach number, and temperature with different phases of flight from the operating conditions of Dong et al. have revealed significant differences in thermal stress trends on the mixing duct.

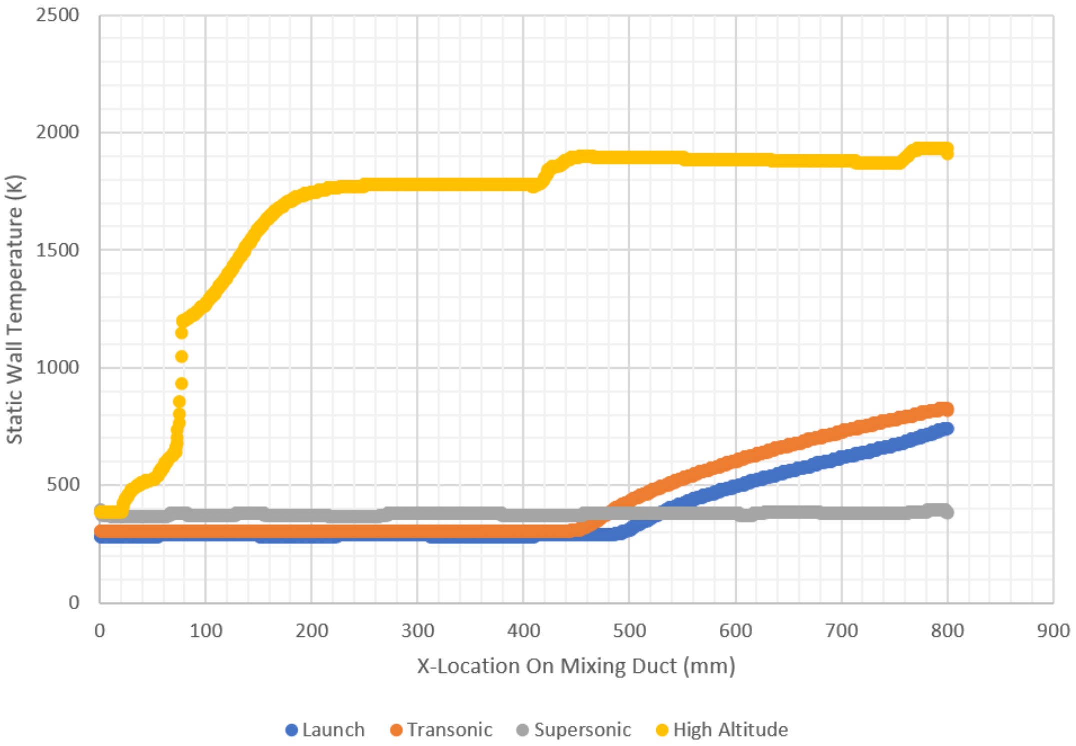

Figure 6.7 Wall Temperature Distribution under Varying Flight Conditions

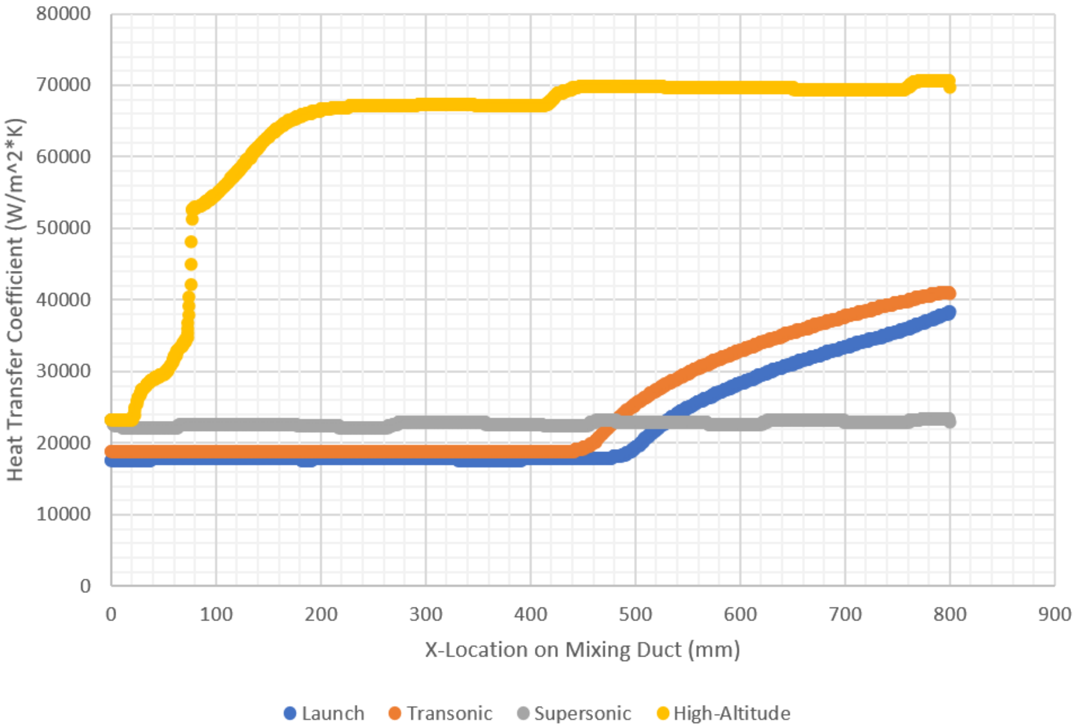

Figure 6.8 Wall Heat Transfer Coefficient vs. Length for Different Phases of Flight

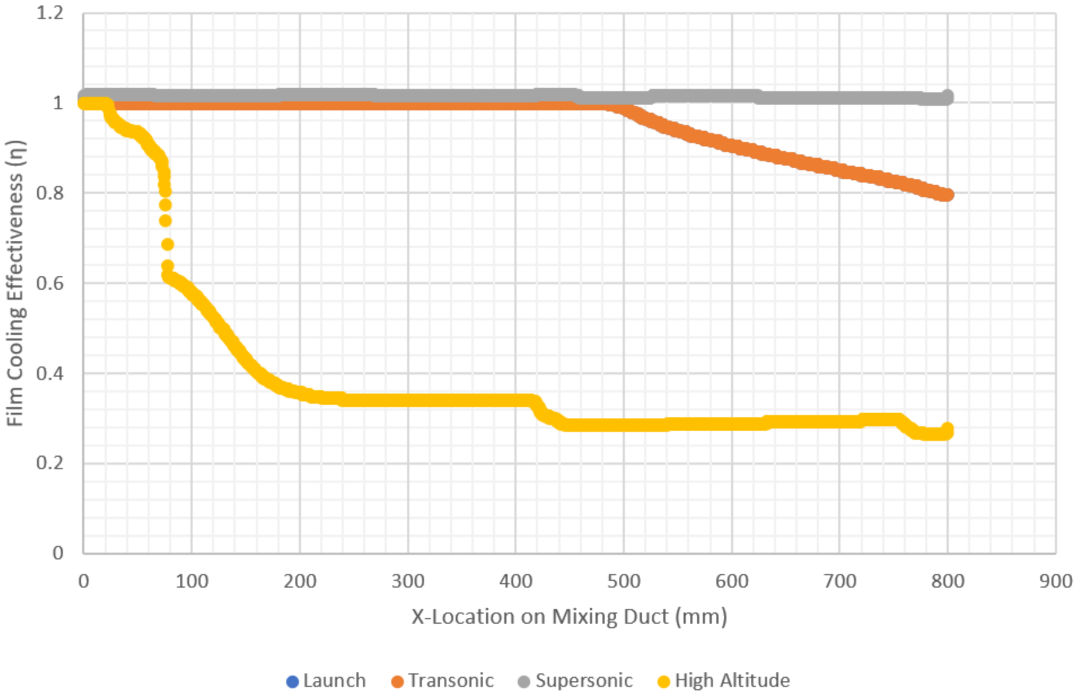

Figure 6.9 Film Cooling Effectiveness vs. Length for Varying Phases of Flight

Table 6.1 Flight Phase and Corresponding Combined Mass Flow Rate of Secondary Inlets

Phase of Flight	Combined Mass Flow Rate of Secondary Inlets ($\frac{kg}{s}$)
Launch	11.41
Transonic	10.94
Supersonic	15.63
High-Altitude	0.2717

6.3 Launch

During launch, the launch vehicle is at an altitude of zero meters with zero forward velocity. Due to the lack of forward velocity, the RBCC engine is acting in the ejector mode. In order to properly model this entrainment behavior in CFD, the geometry for the secondary inlets had to be extended out to allow for the proper development of this low-speed flow.

Air entering the mixing duct from the secondary inlets is entrained by the pumping effects of the rocket exhaust entering the mixing duct [12]. The mass flow rate of air flowing into the mixing duct is limited by the rate at which the primary flow is capable entraining air. For this case, the mass flow rate of air entrained into the mixing duct was 11.41 $\frac{kg}{s}$.

As seen in the contour plots in Figures 6.10, 6.11, 6.12, and 6.13, the rocket exhaust is over-expanded at launch. A pattern of Mach diamonds is generated as the primary flow undergoes compression and expansion as seen in the pressure contour plot of Figure 6.13. None of these shocks or expansion fans have any significant impact on temperature, heat transfer coefficient, or adiabatic film cooling effectiveness on the mixing duct until approximately an x-location of approximately 570mm. After this location, the relatively constant temperature of 284K and heat transfer coefficient of 18,000 $\frac{W}{m^2K}$ begin to increase rapidly. As indicated by the increased uniformity of the temperature, Mach number, velocity, and pressure contour plots, sufficient mixing has occurred by then that the hot gases of the primary flow begin to have greater interaction with the mixing duct walls.

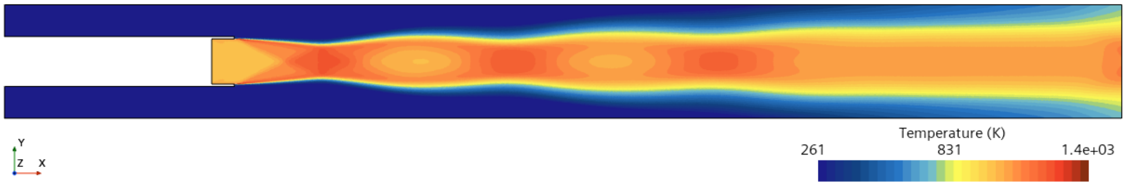

Figure 6.10 Temperature Contour Plot for Launch Case

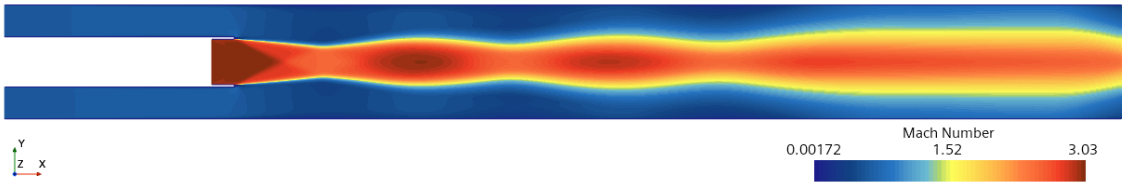

Figure 6.11 Mach Contour Plot for Launch Case

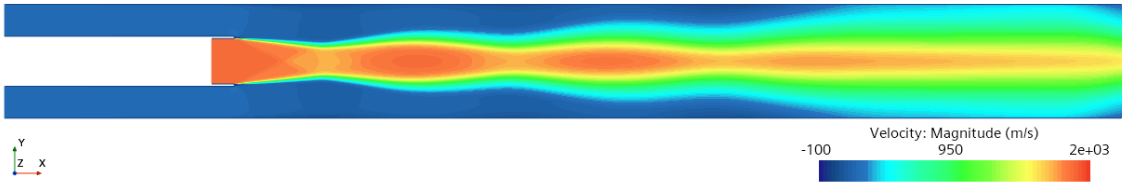

Figure 6.12 Velocity Contour Plot for Launch Case

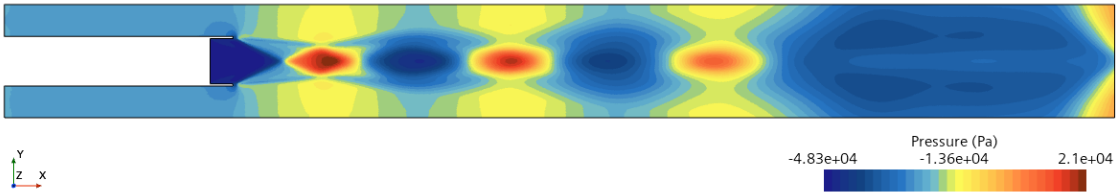

Figure 6.13 Pressure Contour Plot for Launch Case

The solution of the launch case bears a striking similarity to in-flight photos taken and the conditions experienced on Gryphus III. Heating conditions only became severe towards the bottom of the duct when the primary and secondary flows were at a high level of mixing. When Gryphus III was flown with mixing duct $\frac{L}{D}$ values of 8 and 10, this is when the most significant degradation of the mixing duct and was observed. Subsequent flights which utilized lower $\frac{L}{D}$ ducts did not experience any observable degradation to the mixing duct structure or the attached fins.

Despite the low velocity of the secondary flow entering the mixing duct, the adiabatic film cooling effectiveness up to 570mm. is remarkably high as seen in Figure 6.9. Maximum values for wall temperature of 743.4K and a maximum heat transfer coefficient of 38,205.9 $\frac{W}{m^2K}$ were observed in the launch flight case. Along with the results of the temperature contour plot in Figure 6.10, design concerns for high thermal loads should be concentrated towards the aft section of the mixing duct.

6.4 Transonic

At the selected transonic phase of flight, the Mach number of the launch vehicle is 0.944. As with the launch condition, the RBCC engine is still operating in the ejector mode with the pumping action of the primary flow being the main factor responsible for accelerating the secondary flow and raising its stagnation pressure in the mixing duct [12]. With a primary flow static pressure of 53,910 Pa and a secondary flow static pressure of 59,894 Pa at this location in the reference trajectory, the rocket motor is operating in a slightly over-expanded condition. Compared to the launch condition the difference in pressures is considerably smaller, resulting in weaker shocks and expansion fans in the primary flow as seen in the Mach contour plot of Figure 6.15. As illustrated above in Figures 6.7 and 6.8, the static wall temperature and heat transfer coefficient values and trends are very close to that of the launch case. The wall temperature and heat transfer coefficient remain a relatively constant 303K and 18,800 $\frac{W}{m^2K}$ up until 450mm down the mixing duct. The jump in these two parameters begins earlier in the mixing duct than in the launch case.

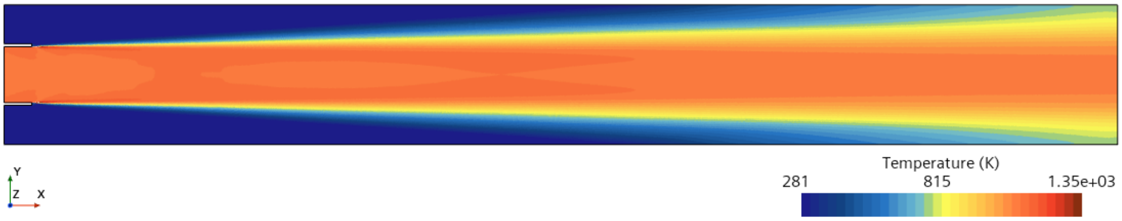

Figure 6.14 Temperature Contour Plot for Transonic Case

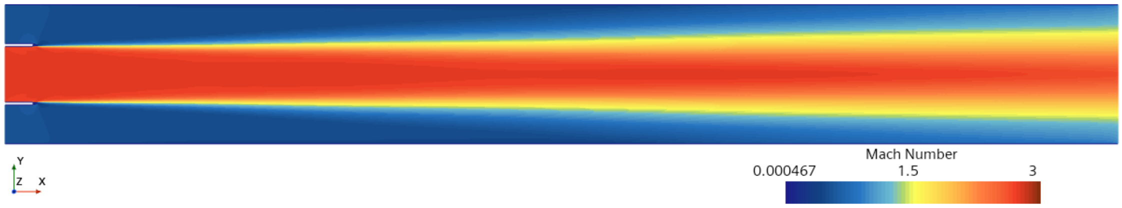

Figure 6.15 Mach Contour Plot for Transonic Case

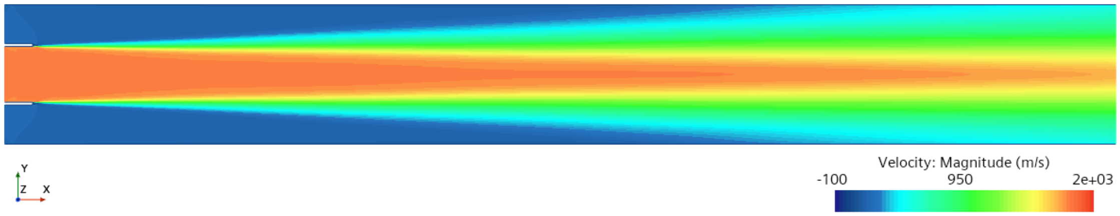

Figure 6.16 Velocity Contour Plot for Transonic Case

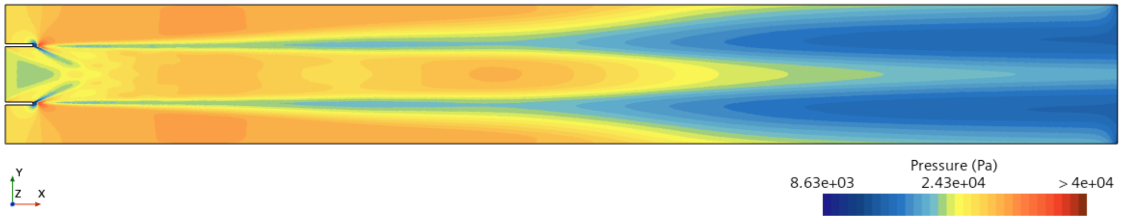

Figure 6.17 Pressure Contour Plot for Transonic Case

Performing a qualitative evaluation of the contour plots in Figures 6.14, 6.15, 6.16, and 6.17, the transonic case seems to encourage much faster development of the turbulent mixing layer. The temperature, velocity, and pressure appear to be more uniform across the height of the mixing duct. It is difficult to distinguish two separate flows by the time the mixture reaches the end of the mixing duct. At the end of the mixing duct the temperature has risen to 819.9K and the heat transfer coefficient reached 40,966 $\frac{W}{m^2K}$. This is a 9.33% and a 6.73 % increase in wall temperature and heat transfer coefficient, respectively. Because of the higher level of mixing that occurs earlier in the mixing duct, a greater length of the aft section of mixing duct wall is exposed to a higher heating environment when compared to the launch case.

Interestingly, the change in film cooling effectiveness along the wall from Figure 6.9 behaves in an almost identical manner to that of the launch case with the curve for the transonic case essentially tracing the launch case. The mass flow rate of air flowing into the mixing duct actually decreased slightly for this case to 10.94 $\frac{kg}{s}$.

6.5 Supersonic

In the supersonic operating case from the reference trajectory, the CFD results seem to yield the overall lowest thermal stress of all the tested phases of flight. Though the wall temperatures are on average higher those seen in the launch or transonic flight cases up until 0.45m in the mixing duct, the maximum wall temperature seen for the supersonic case is 386.5K. The maximum heat transfer coefficient in this case was 22,968.4 $\frac{W}{m^2K}$.This is 48% lower peak wall temperature and a 39% reduction in peak heat transfer coefficient when compared to launch, the flight phase with the next highest thermal loading.

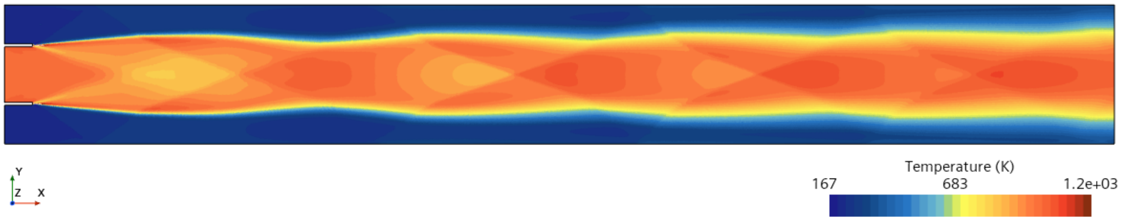

Figure 6.18 Temperature Contour Plot for Supersonic Case

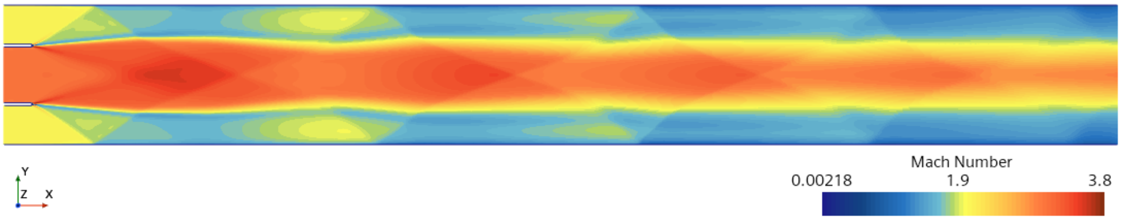

Figure 6.19 Mach Contour Plot for Supersonic Case

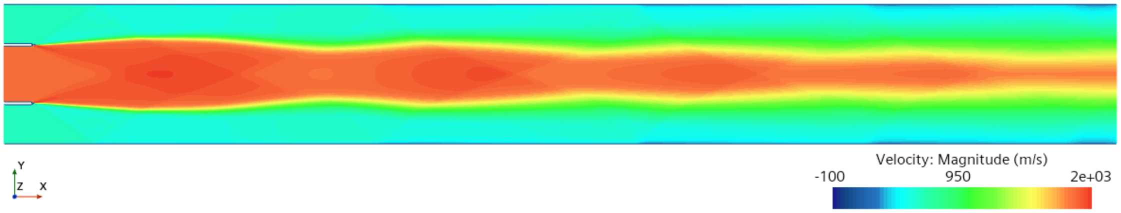

Figure 6.20 Velocity Contour Plot for Supersonic Case

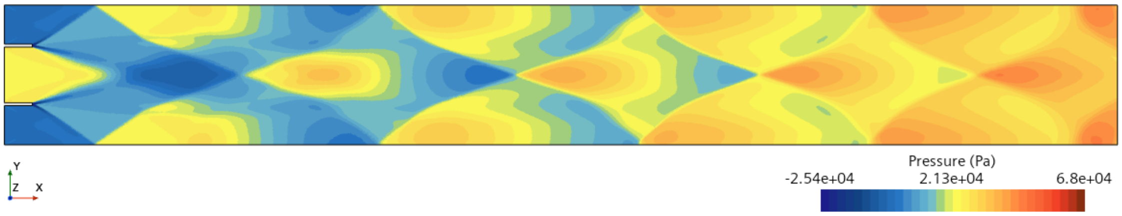

Figure 6.21 Pressure Contour Plot for Supersonic Case

The adiabatic film cooling effectiveness of the supersonic case remains to be approximately $\eta = 1$ for the entire length of the mixing duct. Unlike the launch and transonic cases, the supersonic case did not have location in the mixing duct where temperature and heat transfer coefficient values began to rise rapidly and adiabatic film cooling efficiency dropped quickly. Rather, the values for all three parameters remained essentially constant throughout the length of the mixing duct. Additionally, as opposed to the behaviors seen in the contour plots for the transonic and launch cases, the level of mixing of the primary and secondary flows appear to be lower as two distinct flow paths are present through the entire length of the duct. The high cooling effectiveness observed in this case may be partially attributed to the higher mass flow rate of entrained air. In this case, the model predicted the mass flow rate of secondary flow to be 16.63 $\frac{kg}{s}$. This is the highest of all the different operating cases. The primary flow is under-expanded in this case. Reflecting expansion fans and shocks were observed to interact with the mixing duct walls, but it translated to an insignificant change in thermal conditions along the duct walls.

When factoring the impacts of phase of flight and the corresponding thermal conditions into the design of an RBCC engine, a supersonic condition like the one modelled in this study can be considered one of the least impactful to the mixing duct.

6.6 High-Altitude

The high-altitude altitude case was selected because as the RBCC engine ascends through the atmosphere along the reference trajectory, there comes a point where the operational mode of the engine should change to maintain the highest possible I_{sp}. The location on the reference trajectory selected for the high-altitude phase of flight represents a point at which the air density has decreased substantially from sea-level conditions and operating in air-augmented mode is no longer viable. Assuming a sufficient Mach number is achieved, the goal would be to transition to a ramjet mode and gain the benefits of combusting the fuel stored onboard with atmospheric oxygen.

Referring back to Figures 6.7, 6.8, and 6.9, the thermal conditions imposed on the mixing duct are the most severe of any case in this study. The temperature, heat transfer coefficient, and film cooling effectiveness rapidly change very early on in the mixing duct. By the time the flow reached an x-location of 780mm, they rose dramatically. Peak values for wall temperature and heat transfer coefficient reach 1,935.7 K and 70,734.7 $\frac{W}{m^2 K}$. This is a 57.6 % higher peak wall temperature and a 42.1 % higher heat transfer coefficient than the next highest heating conditions of the transonic case.

The film cooling effectiveness for the high-altitude case is also very low compared to the other phases of flight. Most of the length of the mixing duct walls have a film cooling effectiveness of under $\eta = 0.6$ and this value drops to $\eta = 0.267$ at the end of the mixing duct. The natural cooling ability of the secondary air is insufficient to cool the mixing duct walls. In this phase of flight, the secondary inlets only ingest a mass flow rate of 0.2717 $\frac{kg}{s}$ into the mixing duct. This, combined with the primary flow being severely under-expanded at this altitude, significantly limits the ability of the mixing duct wall to be cooled.

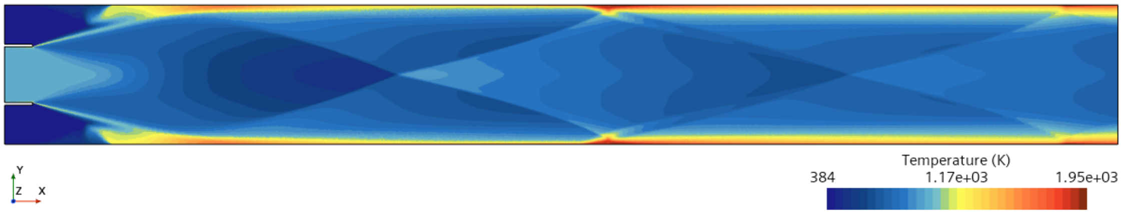

Figure 6.22 Temperature Contour Plot for High Altitude Case

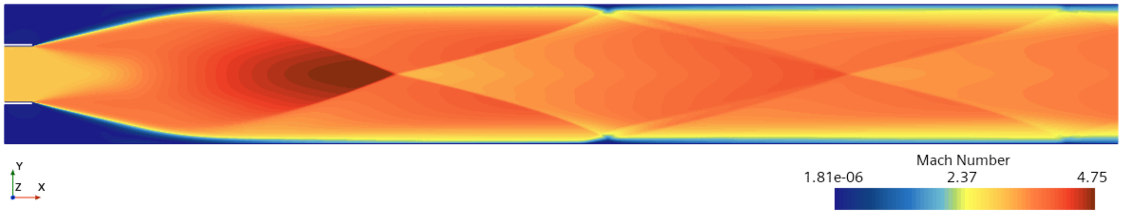

Figure 6.23 Mach Contour Plot for High Altitude Case

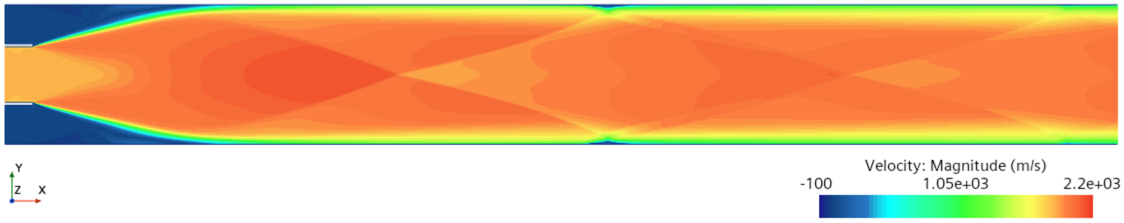

Figure 6.24 Velocity Contour Plot for High Altitude Case

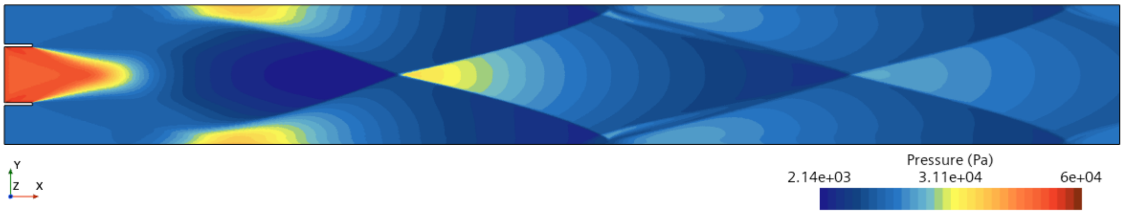

Figure 6.25 Pressure Contour Plot for High Altitude Case

The contour plots above illustrate the expansion of the primary flow plume as it enters the mixing duct. Shocks can be seen reflecting off the walls after the plume first strikes the walls. In the temperature contour plot, it appears as though the initial expanding plume from the primary flow compresses the secondary flow up against the mixing duct walls. After this initial expansion, the primary flow plume continues to occupy almost all of the mixing duct area through the end of the domain. This results in high wall temperatures and heat transfer coefficients with low film cooling effectiveness that span much of the mixing duct length.

7 Conclusion

The investigation into the thermal trends within the mixing duct of a RBCC engine operating in ejector and air-augmented modes has been completed. Motivated by the mixing duct failure of the student-built Gryphus III air-augmented rocket flight vehicle, the thermal trends within the two-dimensional mixing duct of Dong et al. [6]were modelled in CFD. Within this study, nine different mixing duct $\frac{L}{D}$ values as well as four different phases of flight were analyzed. With $\frac{L}{D}$ values ranging from 4-11, the RBCC mixing duct was modeled using the baseline inflow conditions of Dong et al. in STAR CCM+.

Following the analysis of model results, it was found that, from the beginning of the mixing duct up until an $\frac{L}{D}$ value of 7 was reached at an x-position of 700mm, the wall temperature, heat transfer coefficient, and film cooling effectiveness remained relatively constant. After this point, growth of the mixing layer had reached a point where the hot gases of the primary flow were interacting with the wall and resulting in a rise in wall temperature and heat transfer coefficient as well as a decrease in film cooling effectiveness. Mixing duct lengths with $\frac{L}{D}$ values of 8.5 were considered ideal for maximizing mixing and promoting high propulsive efficiency [10]. This study, however, indicates that mixing ducts with $\frac{L}{D}$ of greater than 7 will encounter high thermal stresses in the aft end of the mixing duct. This makes mixing duct designs featuring lower $\frac{L}{D}$ values will benefit from lowered operating temperatures.

Furthermore, the second part of the study was completed focusing on the effects of different phases of flight on the thermal trends experienced by the mixing duct. In this study, the baseline geometry from Dong et al. [6] was modelled under flight conditions. The launch and transonic cases were found to behave similarly. Benefiting from the air entrained by the pumping action of the primary plume when operating in ejector mode, the mixing duct had relatively low thermal stresses in the regions of the duct where the mixing layer had not fully developed across the entire width of the mixing duct. Thermal stresses only rose in these regions of high mixing when the hot gases of the primary flow had the ability to interact with the mixing duct walls.

The supersonic case yielded the lowest thermal loading of the four flight phases analyzed in this study. Benefiting from a higher mass flow rate of secondary air due to the high velocity of the vehicle and slight overexpansion of the primary flow, the mixing duct experienced almost completely constant wall temperature and heat transfer coefficient. With maximum values for temperature and heat transfer coefficient of 386.5K and 22,968.4 $\frac{W}{m^2K}$ respectively as well a constant film cooling coefficient of η =1, the mixing duct was able to have overall lower heating than the launch or transonic cases.

Of the four flight phases selected from the reference trajectory, the high-altitude case was identified to have the most severe thermal environment for the mixing duct. A highly under-expanded primary flow plume combined with a low mass flow rate of secondary air resulted in wall temperatures as high as 1935.7K and a peak heat transfer coefficient of 70,734.7$\frac{W}{m^2K}$. This combined with a local film cooling effectiveness low of $\eta = 0.267$ resulted in high thermal loading in the mixing duct.

It is hoped that the thermal trends identified from this study, can be applied to the design of future RBCC engines. Future designs should be made with special consideration to avoid the thermal conditions that arise from longer mixing ducts with $\frac{L}{D}$ values of over 7 as well as the high heat conditions present along the mixing duct walls when operating the RBCC engine in ejector mode in a high-altitude, low pressure environment.

8 Recommendations

As this was a preliminary study of thermal trends within an RBCC engine mixing duct, more in-depth analysis should be conducted in order to properly identify the thermal trends for any specific design. Further study of this subject should have the entire RBCC engine modeled, including the inlets. Inlet design will have a large impact on conditioning the secondary flow before it enters the mixing duct.

The different phases of flight chosen for this study were selected from a reference trajectory for a traditional chemical rocket-powered launch vehicle. Trajectories optimized for an RBCC engines should be tested to see if flight conditions specific to those trajectories could create unfavorable thermal conditions within the mixing duct. Additionally, combustion modelling could be employed to investigate thermal trends in RBCC configurations that include afterburning concepts.

Lastly, the configuration selected for this study represents the simplest form of RBCC engine. It was selected because it represented the simplest approach with an unmodified chemical rocket engine retrofitted with an inlet and mixing duct, transforming it into an RBCC engine. Many studies have been published highlighting the use of alternative nozzle configurations such as clustering nozzles, annual nozzles, and concentric nozzles. Though this would require specially built thrust chambers and not allow for conventional chemical rocket engines to be used in some cases, these configurations promise mixing duct $\frac{L}{D}$ values far smaller than any single rocket nozzle configuration could provide. A mixing duct this short would potentially allow for the thermal trends identified in this study to be avoided all together.

REFERENCES

[1] Gu, R., Sun, M., Cai, Z., Li, P., and Huang, Y., "Numerical modeling and experimental investigation on the rocket-ejector system with limited mixer length," *Acta Astronautica*, Vol. 182, 2021, pp. 13 – 20. https://doi.org/10.1016/j.actaastrao/2021.01.055.

[2] Ewen, R. L., and Evensen, H., "Liquid Rocket Engine Self-Cooled Combustion Chambers," 1977.

[3] Huzel, D., and Huang, D., *Modern Engineering For Design of Liquid-Propellant Rocket Engines*, Progress in Astronautics and Aeronautics, American Institute of Aeronautics and Astronautics, 1992.

[4] Terry, J. E., and Caras, G., "Transpiration and Film Cooling of Liquid Rocket Nozzles," 1966.

[5] Herrmann, C., and Koschel, W., "Experimental Investigation of the Internal Compression of a Hypersonic Intake," *38th AIAA/ASME/SAE/ASEE Joint Propulsion Conference and Exhibit*, 2002. https://doi.org/10.2514/6.2002-4130.

[6] Dong, Z., Sun, M., Wang, Z., Cai, Z., Yizhi, Y., and Gu, R., "Numerical Investigation on Flow and Mixing Characteristics Inside a Converging-Diverging Mixing Duct of Rocket-Based Combined-Cycle Engine in Ejector Mode," *Aerospace Science and Technology*, Vol. 106, 2020. https://doi.org/10.1016/j.ast.2020.106102.

[7] Foster, R. W., Escher, W., and Robinson, J., "Air Augmented Rocket Propulsion Concepts," 1988.

[8] Sutton, G., and Biblarz, O., *Rocket Propulsion Elements: Eigth Edition*, John Wiley Sons, Inc, 2010.

[9] Daines, R., and Segal, C., "Combined Rocket and Airbreathing Propulsion Systems

for Space-Launch Applications," *Journal of Propulsion and Power*, Vol. 14, 1998, pp. 605–612. https://doi.org/10.2514/2.5352.

[10] Dijkstra, J., Maree, A., Caporicci, M., and Immich, H., "Experimental Investigation of the Thrust Enhancement Potential of Ejector Rockets," *American Institute of Aeronautics and Astronautics*, 1997. https://doi.org/10.2514/6.1997-2756.

[11] Etele, J., and Sislian, J., "Effect of Rocket Exhaust Configurations on Ejector Performance in RBCC Engines," *Journal of Power and Propulsion*, Vol. 2005, 2005, pp. 656–666. https://doi.org/10.2514/1.10794.

[12] Brevig, O., "A Simplified, Preliminary Comparison between the Ejector Ramjet and the Shrouded Rocket," 1968.

[13] Waung, T. S., "An Ejector Air Intake Design Method for a Novel Rocket-Based Combined-Cycle Rocket Nozzle," Master's thesis, Carleton University, Ottawa, Ontario, Canada, 2010.

[14] Escher, W., "A Study of Composite Propulsion Systems for Advanced Launch Vehicle Applications Volume 3(Part 2 of 2): Main Technical Report, Composite Engine Study Contract: NAS 7-377 Project: 5402," Vol. 41, 1966. https://doi.org/10.2514/6.1996-3040.

[15] Gist, D. R., Foster, T., and DeTurris, D., "Examination of Fabri-Choking in a Simulated Air Augmented Rocket," 2007.

[16] Goebel, S. G., and Dutton, J. C., "Experimental Study of Compressible Turbulent Mixing Layers," *AIAA Journal*, 1991, p. 538.

[17] Papamoschou, D., "Analysis of Partially Mixed Supersonic Ejector," *Journal of Propulsion and Power*, Vol. 12, 1996, pp. 736 – 741. https://doi.org/10.2514/3.24096.

[18] Krothapalli, A., Ross, C., Yamomoto, K., and Joshi, M., "Fluid-Acoustic Interactions in a Low Area Ratio Supersonic Jet Ejector," 1993.

[19] Schuchkin, V., Osipov, M., and Thakur, S., "Mixing and Film Cooling in Supersonic Duct Flows," *International Journal of Heat and Mass Transfer*, Vol. 45, 2002, pp. 4451 – 4461. https://doi.org/10.1016/S0017-9310(02)00151-5.

[20] Hombsch, M., and Olivier, H., "Film Cooling in Laminar and Turbulent Supersonic Flows," *Journal of Spacecraft and Rockets*, Vol. 50, 2013, pp. 742 – 753. https://doi.org/10.2514/1.A32346.

[21] "https://docs.sw.siemens.com/documentation/external/PL20200805113346338/en-US/userManual/userguide/html/index.htmlpage/STARCC%MP2FGUID-7DED1D9B-AAA1-48D4-93A0-62B176764E35.html%23," , 2015.

[22] Zikanov, O., *Essential Computational Fluid Dynamics: Second Edition*, John Wiley Sons, Inc., 2019.

[23] Anderson Jr., J., *Fundamentals of Aerodynamics: Fifth Edition*, McGraw-Hill, 2011.

[24] Cengel, Y., and Ghajar, A., *Heat and Mass Transfer: Fundimentals and Applications Fifth Edition*, McGraw-Hill, 2015.

[25] Parker, J., and Povey, T., "Method for Determining Adiabatic Film Effectiveness in Presence of Thermal Boundary Layer," *Annual Review of Turbomachinery*, Vol. 144, 2022, pp. 051010–1 – 051010–17. https://doi.org/10.1115/1.4053021.